UPC **CTTC**

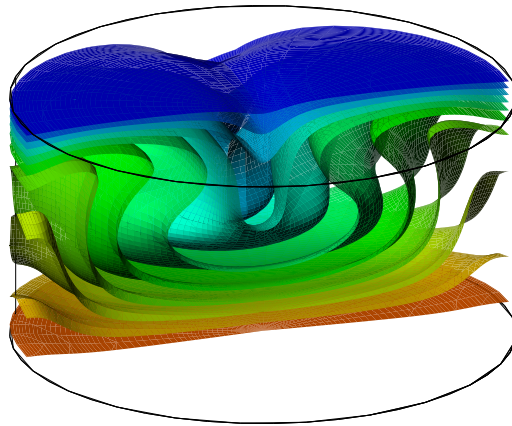# Unsteady laminar convection in cylindrical domains: numerical studies and application to solar water storage tanks

Centre Tecnològic de Transferència de Calor
Departament de Màquines i Motors Tèrmics
Universitat Politècnica de Catalunya

Ivette Rodríguez Pérez
Doctoral Thesis

Unsteady laminar convection in cylindrical domains: numerical studies and application to solar water storage tanks

Centre Tecnològic de Transferència de Calor
Departament de Màquines i Motors Tèrmics
Universitat Politècnica de Catalunya

Ivette Rodríguez Pérez
Doctoral Thesis

Unsteady laminar convection in cylindrical domains: numerical studies and application to solar water storage tanks

Ivette Rodríguez Pérez

TESI DOCTORAL

presentada al

Departament de Màquines i Motors Tèrmics
E.T.S.E.I.A.T.
Universitat Politècnica de Catalunya

per a l'obtenció del grau de

Doctor Enginyer Industrial

Terrassa, December, 2006

Unsteady laminar convection in cylindrical domains: numerical studies and application to solar water storage tanks

Ivette Rodríguez Pérez

Director de la Tesi

Dr. Assensi Oliva Llena

Tribunal Qualificador

Dr. Carlos David Pérez-Segarra
Universitat Politècnica de Catalunya

Dr. Jesús Castro González
Universitat Politècnica de Catalunya

Dr. Antonio Lecuona Neumann
Universidad Carlos III de Madrid

Dr. Agustín Macías Machín
Universidad de Las Palmas de Gran Canaria

Dr. Esteve Codina Macià
Universitat Politècnica de Catalunya

The known is finite, the unknown infinite;
intellectually we stand on an isle in the midst
of an illimitable ocean of inexplicability.
Our business in every generation is to reclaim
a little more land

T.H. Huxley. 1887

a Mamilla
Wish you were here

Acknowledgements

Quisiera aprovechar este espacio para de alguna manera agradecer a todos aquellos que de una forma u otra, intelectual o personal han dejado su huella en esta tesis.

En primer lugar, a Assensi Oliva por haberme dado la oportunidad, ahora hace más de 8 años, de realizar este trabajo, no solo por ser su director, sino también por su apoyo en las más de una dificultades que he tenido que enfrentar a lo largo de estos años. A David (Pérez-Segarra), por tus comentarios siempre oportunos en temas diversos (de transferencia de calor o no) y en particular por la guía en muchos aspectos de esta tesis. En general, a todos mis compañeros del *laboratori*, los presentes y los ausentes, que comenzaron y desarrollaron DPC y sin los que esta tesis no habria podido realizarse. En especial al Ricard Cònsul quien me ayudó a introducirme en el mundo de las coordenadas cilindricas y los tanques de acumulación, al Jordi Cadafalch cuya exigencia y meticulosidad en lo referente al DPC todos hemos "sufrido", al Jesús por haber tenido el valor (y la paciencia) de revisar todo el manuscrito voluntariamente, al Manel y toda una larga lista de compañeros.

Quisiera dar las gracias también a la Generalitat de Catalunya por la beca TDOC que me concedió en el año 2001, para la realización de este trabajo.

En un plano más personal a mis compis de sala que siempre le dan un toque de color a la vida, quizás porque somos una mezcla extraña de nacionalidades y eso, quieras o no, te enriquece.

A todos amigos, los que están lejos y los que de una forma u otra me han ayudado a sentirme *como en casa*. A Jacqui, mi querida hermanita, a Nero, Nely, Su, habeis sido madre, hermana, hija, en una sola palabra *familia*. A Debora y Gus, Conxita, Núria, Vanessa, Ramón y Raquel, Rosa y Santi, Adelina (la meva mare catalana) y en especial al Miquel (trobo a faltar els teus comentaris, consells i la teva amistat).

A la Mercè i el Miquel a qui mai els podré agraïr prou la seva tendresa i el support que m'heu donat en aquests ultims temps, de vegades difícils.

Muy especialmente a mis padres, que siempre apoyasteis cualquier decisión que he tomado, por dura que fuera. Vuestro apoyo y comprehension ha estado siempre presente. A ti mi Mamilla, que te mereces una mención especial, siempre fuiste mi ejemplo, sirvan estas líneas como prueba de que este trabajo está dedicado a tu memoria.

A mi Brego, por tu fidelidad, por hacernos reir y porque consigues que llegar a casa sea siempre una fiesta.

Y por último, pero no menos importante, al Oriol, porque *tú siempre estas ahí*, porque has sabido aceptarme tal como soy y entenderme (!). Sin tí acabar habria sido una pendiente infranqueable.

Contents

Abstract

Thermal storage devices are widely used in many thermal systems and applications that are characterised by the delay between energy production and consumption, such as thermal solar systems. The improvement in their design and optimisation is a key aspect in the thermal optimisation of the system, where a good performance of the storage tank can represent a considerable increase in the overall efficiency of the installation. In the subject of optimisation of thermal equipment, Computational Fluid Dynamics have been consolidated as an indispensable tool providing researchers and engineers with a method to test virtually their prototypes with low effort in time, personnel and resources. This thesis is focused in the numerical simulation of unsteady laminar convection in cylindrical domains and its application to the study of heat transfer and fluid flow that take place in stratified storage tanks.

The methodology followed for the numerical resolution of the governing equation of heat and fluid flow in cylindrical coordinates is presented. The particularities of the discretisation of the equations in these geometries, as well as the solution procedure for incompressible and transient flow problems is also exposed. Special emphasis is given to the verification of the code, the appropriateness of the discretisation adopted and the verification of the numerical solution obtained.

This methodology is used for the study of the heat transfer and fluid flow phenomena that take place in stratified storage tanks, including the performance measures and modelling efforts of these devices. A key aspect in the performance of the tanks is the quality of the energy stored, which is determined by the degree of the thermal stratification of the storage tank. Thermal stratification is affected by several factors such as the mixing due to the inlet streams during load and unload, the heat losses to the environment, among others. In order to analyse the behaviour of the fluid under different working conditions and tank configurations, the virtual prototyping of these devices is carried out. Different parameters for measuring the performance of the tank are considered. This analysis led to the proposition of a non dimensional exergy-based parameter as a tool for assessing and comparing storage tanks. The usefulness of this parameter for quantifying the quality of the energy stored is also shown.

Furthermore, the thermal behaviour of storage tanks during the static mode of operation considering the heat losses to the environment is also analysed. The study is addressed to characterise the cool down of the fluid inside storage tanks for solar thermal systems in the low-to-medium temperature range. The methodology followed, from the identification of the significant non-dimensional parameters that define the problem, the formulation of a zonal prediction model, a parametric numerical study by means of detailed multidimensional CFD computations and the

post-processing of the results in order to obtain the correlations for the heat transfer coefficient and the mean fluid temperature to feed the global model, are exposed in detail. The zonal model presented, together with the correlations given are in good agreement with the numerical results and constitute an alternative for the prediction of the long-term performance of storage tanks during their static mode of operation.

Chapter 1

Introduction

1.1 Prologue

Thermal storage devices are widely used in most of the thermal system where there is an intermittent energy source to meet the demand, or in those systems with a certain delay between production and energy consumption. Many sectors in engineering, such as petroleum, chemical industry, food industry, solar energy systems, industrial processes, refrigeration and air conditioning, among others, require the use of thermal storages to optimise the performance of their systems.

It is important the mode of energy storage, i.e. whether the energy is stored: by means of a heat of reaction in a reversible chemical reaction, by means of sensible heat in a liquid or solid medium or by means of latent heat as the latent heat required for a phase change of the storage material. In the latter, the temperature at which the phase change occurs is of importance because it must be compatible with the temperature of the system.

Regarding to sensible heat storage, its main characteristic is the heat capacity of the storage medium. Because of their simplicity and relative low cost, this type of equipment has emerged as the most widely used in thermal systems. Within the wide range of sensible storage medium, storage tanks of liquid water are routinely used in standard thermal solar systems (e.g. solar domestic hot water and heating). Water, due to its abundance, low cost and good thermal properties (high specific heat capacity and relative high density) is the most attractive choice as storage medium in the low-to-medium temperature range.

In most of the solar thermal energy systems, water is heated during the day and stored for use during the daytime or nighttime, extending the use of solar energy over a larger part of the day. The main objective of the storing process is to maintain the thermodynamic availability of the stored energy to allow its extraction at the same temperature level at which it was stored. In addition, in low-to-medium solar energy systems, the moderate range of working temperature involved limits
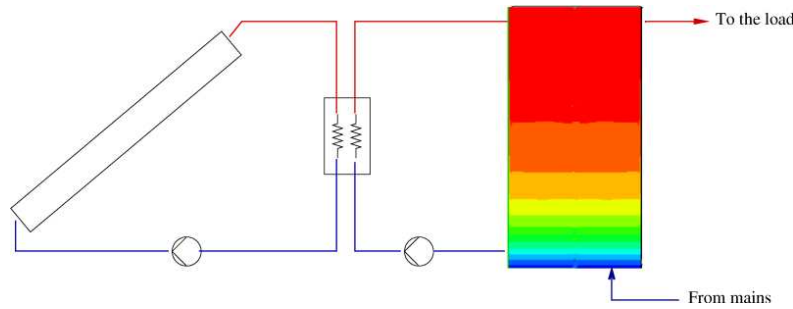
Figure 1.1: Schematic of a solar domestic hot water system with a stratified storage tank.

the storage capacity. Thus, the storage of a large amount of energy requires relative large tanks. These devices must be therefore, simple in operation, cheap in maintenance and cost and reliable. All these characteristics made stratified storage tanks the most attractive choice to achieve the best performance with a low cost in most of solar energy systems.

Thermal stratified storage tanks

The principle of operation of stratified storage tanks is based on the natural process of stratification. In these devices, the cold fluid is withdrawn from the bottom to be heated at the heat source, e.g. solar collectors, and returned to the top of the tank at a relative higher temperature (see Fig. 1.1). As a result, a temperature difference between the top and the bottom parts of the tank arises with the consequent variation of the density in the medium. At the inlet zone appears a mixing fluid region that is gradually pushed down as more fluid enters the tank. As a consequence, a region with a steep temperature gradient is formed, which is known as the *thermocline* region. Once the *thermocline* is developed, it travels down as the charging process continues, limiting the mixing between the cold and the hot regions. In fact, the thickness of the thermocline has been used as a means of quantifying how well a stratified tank has been designed [1, 2]. The higher the mixing at the inlet, the thick the thermocline zone.

However, during the operation of a solar system, not always the temperature of the water entering the tank is greater than the temperature of the fluid at the inlet zone. In those situations, flow entering the tank seeks the level most closest to its temperature resulting in a buoyant flow that enhances the mixing in the storage tank.

1.1. Prologue

Thermal stratified storage tanks are an effective management technique to improve the efficiency of the system [3, 4]. Stratification improves the overall performance of the systems by increasing the efficiency of solar collectors (reducing the average collector absorber plate temperature). Improvements in yearly performance of solar energy systems have been reported in the literature [4, 5]. As an example of this increase in system annual performance due to the stratification of the tank, the simulation of a domestic hot water system has been done. Simulations have been carried out with a prediction code named *SOLCODE* [6] and assuming two situations: an ideally stratified and a fully mixed tank models. *SOLCODE* is a pseudo-transient prediction code developed at the Heat and Mass Transfer Technological Centre (CTTC) of the Technical University of Catalonia (UPC). *SOLCODE* is based on one-dimensional or zero-dimensional models of the components of the systems, which has the capability of interconnect each component, solving the resulting system of equations, and providing long-term predictions results. In the example, the the system considered has a collector area of $4m^2$ and a storage device of $0.3m^3$. The daily load consumption has been taken as one renovation of the tank per day with a load profile proposed by [7] and the consumption temperature of $60°C$. The system has been modelled for Barcelona climate [8]. Results of the simulations have shown improvements in annual system solar fraction of the ideally stratified tank respect the fully mixed around 15%. The advantage of stratified solar tanks, has, of course, been overestimated in the above calculations. Real storage tanks are neither perfectly stratified nor perfectly mixed.

Temperature stratification, however, is characterised by its extreme weakness. There are several factors associated with the loss of stratification in a thermal liquid storage tank. The most important ones are:

- The mixing produced by the inlet streams during the load or withdrawn phases. This can be considered the major cause of destratification.

- The heat losses to the ambient through the tank envelope.

- Heat conduction from the hot layers to the cold layers.

- Thermal bridges along the tank walls, which together with heat losses to the environment produces convective currents that promote mixing.

Due to all the phenomena associated, stratified storage tanks have been subject of many experimental and theoretical works. Most of these studies have been focused in the improvement of the degree of thermal stratification: study of the inlet and outlet ports [9, 10], influence of different kind of diffusers [11, 12, 13, 14, 15, 16], reduce thermal bridges and heat losses to the ambient [17, 18, 19], influence of the mass flow rates [20, 21, 22, 23] among others.

Modelling of thermal storage tanks

The design and optimisation of thermal stratified storage tanks require a profound knowledge of the thermal and fluid dynamic phenomena involved. The complex phenomena associated with the behaviour of these devices, make optimised design a challenge for researchers and designers. In spite of these optimisation difficulties, designs are very often based on simple mathematical models (analytical methodologies based on global mass and energy balances or one-dimensional models), and expensive experimental trial-and-error analysis using prototypes to provide the necessary information for these models (i.e. heat transfer coefficient in convection, pressure loss coefficient, mixing parameters, etc.).

The importance of one-dimensional models relays in the fact that they are computationally more efficient in terms of CPU time cost and suitable for use into overall energy-system simulation programs which allow long-term studies. For this reason, one-dimensional modelling has been the focus of attention of many researchers. A great number of simplified models to account for stratification have been developed. Some of these models are based in the multinode approach [7], being the degree of stratification determined by the choice of the number of temperature levels. Different modifications to this model to account for the mixing at the inlet ports such as those proposed by [24], have been later introduced. Other kind of one-dimensional approaches to account for this mixing have been proposed in the literature [25, 12, 26, 27]. The main problem of those models is the necessity of empirical-based information to evaluate mixing at the inlets. Thus, the validity of such results depends on the accuracy of the experimental coefficients and their suitability for the models.

On the other hand, detailed models with less use of experimental coefficients are capable of describing the thermal and hydrodynamic behaviour of the case of study. Detailed numerical simulations of heat transfer and fluid flow using Computational Fluid Dynamics (CFD) codes have emerged in the recent years as a powerful alternative tool for the prediction of the behaviour of thermal systems and equipment. These codes can give accurate results and thus, can be used for the assessment of the design of innovative concepts. In addition, the results of these detailed codes, can also be used as a source to feed the aforementioned global (or prediction) models.

CFD simulations provide the designer with a way to test the equipment virtually, which is actually known as *Virtual Prototyping*. According with the definition given by [28]:

> *"Virtual prototype, or digital mock-up, is a computer simulation of a physical product that can be presented, analysed, and tested from concerned product life-cycle aspects such as design/engineering, manufacturing, service, and recycling as if on a real physical model. The construction and testing of a virtual prototype*

> *is called virtual prototyping (VP)"*

Such virtual prototyping can shorten design/test cycles and reduce costs. This would enable the analysis of, in the case of storage tanks, the optimum location of inlet/outlet ports, the improvements obtained using particular kinds of diffusers, or the thermal behaviour of inner heat exchangers. However, detailed numerical simulations demand large computational resources.

Numerical simulations of storage tanks can be sometimes very difficult due to their huge computational cost (three-dimensional transient simulations). Although the increase in computational power and the improvement of the numerical methods have been significant over the last few decades, and many engineers and technicians have started to use CFD codes on their desktop computers, the numerical resolution of transient three-dimensional CFD problems using standard PCs is still nowadays computationally very costly.

Taking into account this limitation, and the particularly high cost of fast sequential computers (which require special hardware with a reduced market), parallel computing systems seem to be the most attractive option for the near future. This is especially true considering the emergence of a new class of low cost and loosely coupled parallel computers: the so-called *Beowulf clusters* [29] of personal computers running under Linux Operative System [30]. In order to take advantage of these "low cost" parallel computers and use them efficiently, parallel algorithms that tolerate slow networks are currently being developed.

1.2   Background

The present thesis has been developed at the Heat and Mass Transfer Technological Centre (CTTC) of the Technical University of Catalonia (UPC). CTTC is devoted to the mathematical formulation, numerical resolution and experimental validation of heat and mass transfer phenomena and, at the same time, the application of the acquired know-how to the design and optimisation of thermal systems and equipment. The knowledge acquired on these topics has allowed the development of a general purpose CFD code named DPC [31]. DPC is a library for the resolution of combined heat and mass transfer problems by means of computational fluid dynamics using finite volume techniques [32, 33, 34, 35, 36, 37].

Within DPC framework, this thesis focuses on the simulation of the unsteady laminar convection in cylindrical domains and its application to the study of the heat transfer and fluid flow phenomena that take place in water storage tanks for solar thermal systems in the low-to-medium temperature range. In the particular case of the mathematical formulation and resolution of problems in these kind of domains, the basis of the present work can be found in two main research PhD theses

conducted at CTTC: the PhD theses presented by A. Ivancic [38] and by J. Mora [39]. The first is devoted to the mathematical formulation and resolution of natural and forced convection problems applied to cylindrical storage devices. The latter deals with the development of numerical algorithms for solving problems on sequential or parallel computers including the resolution of cases in cylindrical coordinates. The main contributions of these PhD research works on the resolutions of cylindrical coordinates domains and in particular, on the optimisation and design of storage tanks, constitute the starting point for the development of the present thesis.

In any numerical research into heat transfer and fluid flow, verification of the numerical solutions must be considered as an important aspect in order to produce reliable results. In this sense, at CTTC a post-processing procedure for the verification of the numerical results has been implemented [40]. The numerical results are submitted to this verification process in order to assess the numerical uncertainty, necessary to make solutions reliable. This post-processing tool is based on the generalised Richardson extrapolation for *h-refinement* studies and on the Grid Convergence Index (GCI) proposed by Roache [41].

As have been commented before, for the numerical simulation of transient phenomena (e.g fluid flow inside storage tanks has, most of the time, three-dimensional flow configurations), large computational resources are required. In this sense, parallel computing can be an alternative to reduce drastically the huge computational cost of this kind of simulations. CTTC facilities include a loosely coupled Beowulf cluster called Joan Francesc Fernandez (JFF). Nowadays, it is compound of 125 CPU's with 100 Gbytes of RAM memory and 7.25 Tbytes of disk space. Moreover, domain decomposition techniques have been developed to increase the number of grid nodes or solve complicated domains. These techniques are suitable for implementing on parallel computers allowing to solve cases that require a high number of control volumes to obtain accurate solutions. Main contributions on multiblock techniques and parallel computing algorithms can be found in [34] and the PhD theses of M. Soria [30] and J. Mora [39].

The solar energy field constitutes one of the main applied research topics at CTTC. There is an extense *know-how* acquired on different areas within this framework. The main research works carried out have been on the subjects of passive solar energy systems (e.g. multifunctional ventilated facades) [42, 43] and on active solar energy systems with special emphasis on solar collectors [44, 45], storage tanks [38, 46, 47, 23, 16, 19] and solar cooling [48, 49]. In this sense, the expertise obtained on this area has allowed the development of specific prediction codes: *AGLA* [50] which allows the design and optimisation of multifunctional ventilated facades and, *SOLCODE* [6] for the design, optimisation and long-term prediction of active solar heating systems and its components.

A more extense information about reasearch activities (projects and publications)

carried out within the fundamental working lines at CTTC can be found at [51].

1.3 Outline

The main objective of this thesis is the numerical resolution of heat transfer and fluid flow problems in cylindrical coordinates and its application to the study of the unsteady simulation of the convection phenomena in storage devices for solar thermal systems in the low-to-medium temperature range. Next chapter is devoted to present the methodology employed for the resolution of Computational Fluid Dynamics (CFD) and Heat Transfer problems with special emphasis in two and three-dimensional cylindrical coordinates. First, the basic discretisation of the governing equations for cylindrical coordinates based on finite volume techniques (FVM) on staggered grids is presented. Numerical techniques such as the discretisation schemes, boundary conditions implementations and solution procedure for incompressible and transient flow problems is reviewed. Attention is focused on the most relevant particularities of the discretisation in cylindrical coordinates: the special treatment implemented for the singularity that appears at the cylinder centre and, the periodic boundary condition employed in order to solve cylindrical closed domains. Closing the chapter, code and numerical solution verification techniques are exposed. In this sense, a post-processing tool based on the generalised Richardson extrapolation method and on the Grid Convergence Index (GCI) is employed [40].

The *third chapter* is dedicated to discuss the task carried out in order to verify the code and the appropriateness of the adopted discretisation for the treatment of the singularities in cylindrical coordinates domains. Different test cases are submitted to a process of verification of the numerical solutions by means of the techniques described in *Chapter 2*. After a rigorous post-processing of all cases presented, verified solutions for two and three dimensional steady-state problems in cylindrical coordinates are provided. The cases solved are: a flow induced by a tangential velocity at the boundary; the natural convection of a fluid in a cylindrical enclosure heated from below, and the fluid motion between two concentric rotating cylinders. The most relevant results for velocity and temperature fields together with their uncertainty estimates are given. Verified numerical solutions provided can be useful as reference solutions in the process of development of CFD codes in cylindrical coordinates.

Chapter 4 and 5 are focused on the study of transient phenomena in storage tanks. *Chapter 4* is mainly dedicated to the thermal stratification of storage tanks and its degradation due to the inlet mass flow rates. Part of the contents presented in this chapter have been published as [23]. The current state-of-the-art in the analysis of stratified storage tanks is briefly reviewed. Detailed numerical simulations are carried out in order to study different cases and working conditions. From this

analysis a new exergy-based parameter in order to quantify the thermal stratification inside the storage tank is proposed. The current computational possibilities of three-dimensional Computational Fluid Dynamics (CFD) simulations, using loosely coupled parallel computers (Beowulf clusters) for the *virtual prototyping* of thermal storage tanks is also shown.

The static operation mode of a storage tank, where heat losses through the walls is the only mechanism of fluid movement inside the storage, is of particular interest since it represents a frequent state of the tank. In *Chapter 5*, the transient natural convection during the cooling process of a storage tank in this operation mode is analysed. In order to identify the relevant parameters that define this transient natural convection phenomenon, a non-dimensional analysis of the governing equations is performed. This analysis has shown that the transient cooling down of the fluid, taking into account the limiting walls and insulation material, is dominated by the Rayleigh number (Ra), the aspect ratio (H/D) and a non-dimensional overall heat transfer coefficient that accounts for the solid walls ($\widehat{U}$).

A global model analysis to characterise the long term behaviour of the tank including heat losses to the environment is developed. The global model is based on a one-temperature level. Heat losses to the environment are described by means of a transient mean Nusselt number. A parametric study is carried out in order to correlate the transient heat transfer coefficient to the relevant parameters. The main tasks accomplished for the correlation of the results by means of curve-fitting techniques are described. At the end of the chapter, other model possibilities to account for heat losses through each wall independently, are also exposed.

A final chapter with the conclusions of the work performed in this thesis, the main achievements and limitations of the studies carried out, is presented. The guidelines for future research work in this applied area are also suggested.

References

[1] W. P. Bahnflet and A. Musser. Thermal performance of a full-fcale stratified chilled water thermal storage tank. *ASHRAE Transactions*.

[2] A. Musser and W.P. Bahnfleth. Parametric study of charging inlet diffuser performance in stratified chilled water storage tanks with radial diffusers: Part 2-Dimensional analysis, parametric simulations and simplified model development. *HVAC and Research*, 7(1):51–65, 2001.

[3] Sharp M.K. and Loehrke R.I. Stratified thermal storage in residential solar energy applications. *Energy*, 3:106–113, 1979.

References

[4] M. D. Wuesling, S. A. Klien, and J. A. Duffie. Promising control alternatives for solar water heating systems. 107:215–221, 1985.

[5] K.G.T Hollands and H.F. Lightstone. A review of low-flow, stratified tank solar water heating systems. *Solar Energy*, 43:97–106, 1989.

[6] CTTC-UPC. SOLCODE: Solar thermal systems design Code. Developed at the Heat and Mass Transfer Technological Centre (CTTC). Universitat Politècnica de Catalunya.

[7] E.M. Kleinbach, W.A. Beckman, and S.A. Klein. Performance study of one-dimensional models for stratified thermal storage tanks. *Solar Energy*, 50(2):155–166, 1993.

[8] Atlas de radiacio solar a Catalunya. Technical report, Institut Català d'Energia, 2000.

[9] P.C. Eames and B. Norton. The effect of tank geometry on thermally stratified sensible heat storage subject to low Reynolds number flows. *International Journal of Heat and Mass Transfer*, 41(14):2131–2142, 1998.

[10] L. Jivan and S. Furbo. Entrance effects in solar storage tanks. *Solar Energy*, 75:337–348, 2003.

[11] M. W. Wilding. Diffuser design for naturally stratified thermal storage. *ASHRAE Transactions*, 96(1):1094–1102, 1990.

[12] A.J. Ghajar and Zurigat Y.H. Numerical study of the effect of inlet geometry on stratification in thermal energy storage. *Numerical Heat Transfer, Part A*, 19:65–83, 1991.

[13] A. Musser and W.P. Bahnfleth. Parametric study of charging inlet diffuser performance in stratified chilled water storage tanks with radial diffusers: Part 1-Model development and validation. *HVAC and Research*, 7(1):31–65, 2001.

[14] S-Z. Kuhn, H. K. Kang, and P. F. Peterson. Study of mixing augmentation of natural convection heat transfer by a forced jet in a large enclosure. 124:660–666, 2002.

[15] A. Zachar, I. Farkas, and F. Szlivka. Numerical analyses of the impact of plates flor thermal stratification inside a storage tank with upper and lower inlet flows. *Solar Energy*, 74:287–302, 2003.

[16] R. Cònsul, I. Rodríguez, K. Claramunt, and A. Oliva. Thermal stratification improvements in thermal storage tanks: Numerical analysis of directed inlet mass flow rates strategies. In *Proceedings of the 5th ISES Europe Solar Conference (EUROSUN 2004)*, 2004.

[17] Hess C.F. and Miller C.W. An experimental and numerical study on the effect of the wall in a thermocline-type cylindrical enclosure-I. Experiments. *Solar Energy*, 28(2):145–152, 1982.

[18] Hess C.F. and Miller C.W. An experimental and numerical study on the effect of the wall in a thermocline-type cylindrical enclosure-II. Numerical model. *Solar Energy*, 28(2):153–161, 1982.

[19] Rodríguez, A. Oliva, and C.D. Pérez-Segarra. Numerical study of the transient convection inside solar domestic hot water storage tanks. In *Proceedings of the 6th ISES Europe Solar Congress (EUROSUN 2006)*, Glasgow, 2006.

[20] A. Ivancic, A. Oliva, C.D. Pérez-Segarra, and H. Schweiger. Three-dimensional numerical simulation of liquid thermal storage tanks. In *Proceedings of the ISES Solar World Congress 1993*, volume 5, pages 447–452, 1993.

[21] J.P. Meyer, P.J.A. Raubenheimer, and E. Kruger. The influence of return loop flow rate on stratification in a vertical hot water storage tank connected to a heat pump water heater. *Heat Transfer Engineering*, 21:67–73, 2000.

[22] C. Cristofari, G. Notton, P. Poggi, and A. Louche. Influence of the Flow rate and the Tank Stratification Degree on the Performance of a Solar Flat-Plate Collector. *International Journal of Thermal Sciences*, 42:455–469, 2003.

[23] R. Cònsul, I. Rodríguez, C.D. Pérez-Segarra, and M. Soria. Virtual prototyping of storage tanks by means of three-dimensional CFD and heat transfer simulations. *Solar Energy*, 77(2):179–191, 2004.

[24] S. Alizadeh. An experimental and numerical study of thermal stratification in a horizontal cylindrical solar storage tank. *Solar Energy*, 66(6):409–421, 1999.

[25] Y.H. Zurigat, K.J. Maloney, and A.J. Ghajar. A comparison study of one-dimensional models for stratified thermal storage tanks. *Journal of Solar Energy Engineering*, 111:204–210, 1988.

[26] N.K. Ghaddar. Stratified storage tank influence of solar water heating system tested in Beirut. *Renewable Energy*, 4(8):911–925, 1994.

References

[27] J.E.B. Nelson, A.R. Balakrishnan, and S.S Murthy. Parametric studies on thermally stratified chilled water storage systems. *Applied Thermal Engineering*, 19:89–115, 1999.

[28] Gary Wang G. Definition and review of virtual prototyping. *Journal of Computing and Information Science in Engineering*, 3:232–236, 2002.

[29] http://www.beowulf.org/.

[30] M. Soria. *Parallel multigrid algorithms for computational fluid dynamics and heat transfer*. PhD thesis, Universitat Politècnica de Catalunya, 2000.

[31] CTTC-UPC. DPC: library for the development of programs focussed on the resolution of combined heat and mass transfer problems. Developed at the Heat and Mass Transfer Technological Centre (CTTC). Universitat Politècnica de Catalunya, 2004.

[32] M. Costa, A. Oliva, and C.D. Pérez-Segarra. A three-dimensional numerical study of melting inside a heated horizontal cylinder. *Numerical Heat Transfer, Part A*, 32(5):531–553, 1997.

[33] C.D. Pérez-Segarra, A. Oliva, and M.. Costa. Benchmark of turbulent natural convection in a square cavity. Comparison between different k-ϵ turbulence models. In *Turbulent natural convection in enclosures. A computational and experimental benchmarck study, ed. R.A.W.M. Henkes and C.J. Hoogendoorn, Editions Europeennes Thermique et Industrie*, pages 109–120, 1992.

[34] J. Cadafalch, A. Oliva, C.D. Pérez-Segarra, M. Costa, and J. Salom. Comparative study of conservative and non conservative interpolation schemes for the domain decomposition method on laminar incompressible flows. *Numerical Heat Transfer, Part B*, 35(1):65–84, 1999.

[35] G. Colomer, M. Costa, R. Cònsul, and A. Oliva. Radiant exchange in domains with obstacles using the discrete ordinates method. In *Proceedings of the Third European Congress on Computational Methods in Applied Sciences and Engineering (ECCOMAS)*, pages 1–20, 2000.

[36] R. Cònsul, C.D. Pérez-Segarra, K. Claramunt, J. Cadafalch, and A. Oliva. Detailed numerical simulation of laminar flames by a parallel multiblock algorithm using loosely coupled computers. *Combustion Theory and Modelling*, 7(3):525–544, 2003.

29

[37] C. Orozco, K. Claramunt, R. Cònsul, and A. Oliva. Finite volume computation and verification of fluid flow and heat transfer in domains with moving boundaries. In *Proceedings of the Fourth European Congress on Computational Methods in Applied Sciences and Engineering (ECCOMAS)*, 2004.

[38] A. Ivancic. *Simulación numérica de la convección natural y forzada en recintos cilíndricos. Aplicación a la acumulación de calor y frío*. PhD thesis, Universitat Politècnica de Catalunya, 1998.

[39] J. Mora. *Desarrollo y validación de algoritmos tridimensionales aplicados a la transferencia de calor, masa y mecánica de fluidos en coordenadas cilíndricas*. PhD thesis, Universitat Politècnica de Catalunya, 2001.

[40] J. Cadafalch, C.D. Pérez-Segarra, R. Cònsul, and A. Oliva. Verification of finite volume computations on steady state fluid flow and heat transfer. *Journal of Fluids Engineering*, 124:11–21, 2002.

[41] P.J. Roache. Perspective: a method for uniform reporting of grid refinement studies. *Journal of Fluids Engineering*, 116:405–413, 1994.

[42] D. Faggembauu, M. Costa, M. Soria, and A. Oliva. Numerical analysis of the thermal behaviour of glazed ventilated facades in Mediterranean climates. Part I: Development and validation of a numerical model. *Solar Energy*, 75(3):217–228, 2003.

[43] D. Faggembauu, M. Costa, M. Soria, and A. Oliva. Numerical analysis of the thermal behaviour of glazed ventilated facades in Mediterranean climates. Part II: Application and analysis of results. *Solar Energy*, 75(3):229–239, 2003.

[44] H. Schweiger. *Optimization of solar thermal absorber elements with transparent insulation*. PhD thesis, Universitat Politècnica de Catalunya, 1997.

[45] J. Cadafalch, A. Oliva, G. Van Der Graaf, and X. Albets. Natural convection in a large, inclined channel with asymmetric heating and surface radiation. *Journal of Heat Transfer*, 125(5):812–820, 2003.

[46] I. Rodríguez, R. Cònsul, J. Cadafalch, and A. Oliva. Numerical studies of thermosyphon solar heaters. In *Proceedings of the 3rd ISES Europe Solar Conference (EUROSUN 2000)*, pages 1–9, 2000.

[47] R. Cònsul, I. Rodríguez, and A. Oliva. Three-dimensional simulation of storage tanks by a parallel multiblock algorithm using loosely coupled computers. In *Proceedings of the ISES Solar World Congress 2003*, 2003.

References

[48] J. Castro, L. Leal, C.D. Pérez-Segarra, and P. Pozo. Numerical study of the enhancement produced in absorption processes using surfactants. *International Journal of Heat and Mass Transfer*, 47:3463–3476, 2004.

[49] J. Castro, A. Oliva, C.D. Pérez-Segarra, and J. Cadafalch. Evaluation of a small capacity, hot water driven, air-cooled H_2O-LiBr absorption machine. *Accepted for publication in*. *HVAC and Research*, 2005.

[50] M. Soria et al. Advanced GLAzed facades simulation software (AGLA) technical manual, 1999.

[51] http://www.cttc.upc.edu/.

Chapter 2

On the resolution of two and three-dimensional CFD and heat transfer problems in cylindrical coordinates

Abstract. The aim of this chapter is to expose the methodology employed for the resolution of two and three-dimensional cylindrical coordinates Computational Fluid Dynamics (CFD) and Heat Transfer problems. The most relevant particularities of the discretisation of the governing equations in cylindrical coordinates such as the treatment of the singularity at the cylinder centre or the periodicity at the azimuthal direction are described. Special emphasis has been given to the process of verification of the code verification and numerical solution. In this sense, a post-processing tool based on the generalised Richardson extrapolation method and on the Grid Convergence Index (GCI) is employed.

2.1 Introduction

Nowadays, numerical methods in heat transfer and fluid flow have been consolidated as a powerful tool for the design/optimisation of thermal systems. Computational Fluid Dynamics (CFD) codes are being employed on the improvement of thermal equipment allowing a reduction in terms of developing costs and time. Different commercial CFD codes are available in the market, and many engineers and technicians are using them in their companies. However, and rather than employing commercial codes for which the source code is rarely available, the CFD scientific community usually develops their own codes, thus having a complete freedom of manipulation.

In this chapter, the main governing equations of fluid flow and heat transfer i.e. the conservation of mass, momentum and energy equations are presented. These equations are the necessary tools to deal mathematically with most of engineering applications. The solution of these equations report a detailed information of the fluid flow variables involved in the phenomena studied: the velocity vector ($\vec{v}$), the pressure (p) and the temperature (T) fields.

In the wide range of applicability of CFD computations, the cases where the physical phenomena takes place in cylindrical geometries (e.g. tubes, tanks, etc.) are very common. Considering different discretisation techniques, structured cylindrical grids offer a good agreement in terms of the fitness of the discretisation to the physical domain and the robustness of the method to be employed on the resolution of the set of Partial Differential Equations (PDEs). On the other hand, the geometry of the domain of study has a strong influence in the flow patterns, being suitable to choose the coordinate system which represent this pattern better.

This thesis is devoted to the study of the transient phenomena that occurs in solar domestic hot water storage tanks. Thus, governing equations presented here are written for cylindrical coordinate systems.

The aim of this chapter is to expose the methodology employed for the resolution of Computational Fluid Dynamics (CFD) and Heat Transfer problems, considering two and three-dimensional cylindrical coordinates. The discretisation of the governing equations for cylindrical coordinates, the most relevant particularities of the discretised equations, formulation of the boundary conditions, numerical schemes considered, and also the verification of the code and numerical results techniques are presented.

2.2 Mathematical formulation

The governing equations of heat transfer and fluid flow (i.e. the conservation of mass, momentum and energy equations) considered along this thesis have been for-

mulated considering unsteady two or three-dimensional flow configuration and taking into account the following hypothesis:

- Incompressible and laminar flow

- Newtonian behaviour

- Physical properties constants with the exception of density variations which are treated assuming Boussinesq approximation (relevant in buoyancy terms of momentum equations)

- Viscous dissipation in the energy equation negligible

- Non-participant radiating medium

Under these hypotheses it is possible to cover a wide range of engineering applications and, in particular, a wide range of operating conditions of solar domestic hot water storage tanks. The equations for cylindrical coordinates can be written as:

the continuity equation:

$$\frac{1}{r}\frac{\partial(rv_r)}{\partial r} + \frac{1}{r}\frac{\partial v_\theta}{\partial \theta} + \frac{\partial v_z}{\partial z} = 0 \tag{2.1}$$

the equations of motion (for r, θ and z directions):

$$\rho\left(\frac{\partial v_r}{\partial t} + \frac{1}{r}\frac{\partial(rv_r v_r)}{\partial r} + \frac{1}{r}\frac{\partial(v_\theta v_r)}{\partial \theta} - \frac{v_\theta^2}{r} + \frac{\partial(v_z v_r)}{\partial z}\right) \tag{2.2}$$
$$= -\frac{\partial p_d}{\partial r} + \left[\frac{1}{r}\frac{\partial(r\tau_{rr})}{\partial r} + \frac{1}{r}\frac{\partial\tau_{\theta r}}{\partial \theta} - \frac{\tau_{\theta\theta}}{r} + \frac{\partial\tau_{zr}}{\partial z}\right] - \rho g_r \beta(T - T_{ref})$$

$$\rho\left(\frac{\partial v_\theta}{\partial t} + \frac{1}{r}\frac{\partial(rv_r v_\theta)}{\partial r} + \frac{1}{r}\frac{\partial(v_\theta v_\theta)}{\partial \theta} + \frac{v_r v_\theta}{r} + \frac{\partial(v_z v_\theta)}{\partial z}\right) \tag{2.3}$$
$$= -\frac{1}{r}\frac{\partial p_d}{\partial \theta} + \left[\frac{1}{r^2}\frac{\partial(r^2\tau_{r\theta})}{\partial r} + \frac{1}{r}\frac{\partial\tau_{\theta\theta}}{\partial \theta} + \frac{\partial\tau_{z\theta}}{\partial z}\right] - \rho g_\theta \beta(T - T_{ref})$$

$$\rho\left(\frac{\partial v_z}{\partial t} + \frac{1}{r}\frac{\partial(rv_r v_z)}{\partial r} + \frac{1}{r}\frac{\partial(v_\theta v_z)}{\partial \theta} + \frac{\partial(v_z v_z)}{\partial z}\right) \tag{2.4}$$
$$= -\frac{\partial p_d}{\partial z} + \left[\frac{1}{r}\frac{\partial(r\tau_{rz})}{\partial r} + \frac{1}{r}\frac{\partial\tau_{\theta z}}{\partial \theta} + \frac{\partial\tau_{zz}}{\partial z}\right] - \rho g_z \beta(T - T_{ref})$$

where shear stresses are evaluated considering a Newtonian behaviour by means of Stoke's law:

$$
\begin{aligned}
\tau_{rr} &= 2\mu\left(\frac{\partial v_r}{\partial r}\right) & \tau_{r\theta} &= \tau_{\theta r} = \mu\left(r\frac{\partial(v_\theta/r)}{\partial r} + \frac{1}{r}\frac{\partial v_r}{\partial\theta}\right) \\
\tau_{\theta\theta} &= 2\mu\left(\frac{1}{r}\frac{\partial v_\theta}{\partial\theta} + \frac{v_r}{r}\right) & \tau_{\theta z} &= \tau_{z\theta} = \mu\left(\frac{\partial v_\theta}{\partial z} + \frac{1}{r}\frac{\partial v_z}{\partial\theta}\right) \\
\tau_{zz} &= 2\mu\left(\frac{\partial v_z}{\partial z}\right) & \tau_{zr} &= \tau_{rz} = \mu\left(\frac{\partial v_z}{\partial r} + \frac{\partial v_r}{\partial z}\right)
\end{aligned}
$$

the energy equation:

$$
\frac{\partial T}{\partial t} + \frac{1}{r}\frac{\partial(rv_rT)}{\partial r} + \frac{1}{r}\frac{\partial(v_\theta T)}{\partial\theta} + \frac{\partial(v_zT)}{\partial z} = \frac{k}{\rho c_p}\left(\frac{1}{r}\frac{\partial}{\partial r}\left(r\frac{\partial T}{\partial r}\right) + \frac{1}{r^2}\frac{\partial^2 T}{\partial\theta^2} + \frac{\partial^2 T}{\partial z^2}\right) \quad (2.5)
$$

Notice that components of the heat flux vector entering the unit of volume by conduction have been evaluated by means of the Fourier's law: $\overrightarrow{q} = -k\nabla T$.

All the above equations (mass conservation, momentum conservation in r, θ and z directions and energy conservation) can be written as the so called *convection-diffusion* equation. For cylindrical coordinates this equation can be expressed as:

$$
\overbrace{\frac{\partial\phi}{\partial t}}^{transient\ term} + \overbrace{\frac{1}{r}\frac{\partial(rv_r\phi)}{\partial r} + \frac{1}{r}\frac{\partial(v_\theta\phi)}{\partial\theta} + \frac{\partial(v_z\phi)}{\partial z}}^{convective\ term} \quad (2.6)
$$

$$
= \Gamma\overbrace{\left[\frac{1}{r}\frac{\partial}{\partial r}\left(r\frac{\partial\phi}{\partial r}\right) + \frac{1}{r^2}\frac{\partial^2\phi}{\partial\theta^2} + \frac{\partial^2\phi}{\partial z^2}\right]}^{diffusive\ term} + \overbrace{S_\phi}^{source\ term}
$$

Equation 2.6 is a balance between the generation, accumulation and transport (by diffusion or convection) of a generic variable ϕ. The terms in the *convection-diffusion* equation are summarised in Table 2.1 depending of which equation is represented.

2.3 Discretisation of the governing equations

In this thesis the governing equations have been approximated by means of a fully-implicit finite volume control method (FVM), based on the conservation fluxes of the primitive variables [1]. The method has been applied on cylindrical staggered grids. To do so, first the whole domain has been discretised into a finite number of

Equation	ϕ	Γ	S_ϕ
Mass conservation	1	0	0
Momentum conservation (r)	v_r	$\dfrac{\mu}{\rho}$	$-\dfrac{1}{\rho}\dfrac{\partial p_d}{\partial r} - g_r\beta(T - T_{ref}) + \dfrac{v_\theta^2}{r} - \dfrac{1}{\rho}\dfrac{\tau_{\theta\theta}}{r}$
Momentum conservation (θ)	v_θ	$\dfrac{\mu}{\rho}$	$-\dfrac{1}{r\rho}\dfrac{\partial p_d}{\partial \theta} - g_\theta\beta(T - T_{ref}) + \dfrac{v_r v_\theta}{r}$
Momentum conservation (z)	v_z	$\dfrac{\mu}{\rho}$	$-\dfrac{1}{\rho}\dfrac{\partial p_d}{\partial z} - g_z\beta(T - T_{ref})$
Energy conservation	T	$\dfrac{k}{\rho c_p}$	$\dfrac{S_T}{\rho c_p}$

Table 2.1: Terms of the generic *convection-diffusion* equation for cylindrical coordinates system

non-overlapped control volumes (CV). This primary grid has been denoted as the centred grid. Additionally, three staggered grids have been defined in each direction of the coordinate system (i.e. for r, θ and z directions). Scalar variables (p_d, T) have been evaluated at the centred grid, while velocity components (v_r, v_θ, v_z) have been evaluated on the staggered grids in each direction (r, θ, z). In Fig. 2.1 there is a representation of the typical control volume for cylindrical coordinates. The value of the variable at the nodal point P, ϕ_P, and the relation with its neighbours ϕ_W, ϕ_E, ϕ_S, ϕ_N, ϕ_B and, ϕ_T is represented. The subscript E and W denotes relative position respect to the nodal point P ($E \rightarrow$ east, $W \rightarrow$ west). In the same manner, N, S, T and B, denote nord, south, top and bottom respectively.

In order to explain the integration of the governing equations in the defined grids, the general *convection-diffusion* equation (Eqn. 2.6) has been used. This equation can be written also as:

$$\frac{\partial \phi}{\partial t} + \nabla \cdot (\mathbf{u}\phi) - \nabla \cdot (\Gamma \nabla \phi) = S_\phi \tag{2.7}$$

It is useful to consider a total flux $\mathbf{J}$ that contains the convective flux ($\mathbf{u}\phi$) and the diffusive flux ($-\Gamma \nabla \phi$). Thus,

$$\mathbf{J} = \mathbf{u}\phi - \Gamma \nabla \phi \tag{2.8}$$

With this definition, the *convection-diffusion* equation 2.7 becomes:

$$\frac{\partial \phi}{\partial t} + \nabla \cdot \mathbf{J} = S_\phi \tag{2.9}$$

Equation 2.9 can be integrated for each control volume in the following manner:
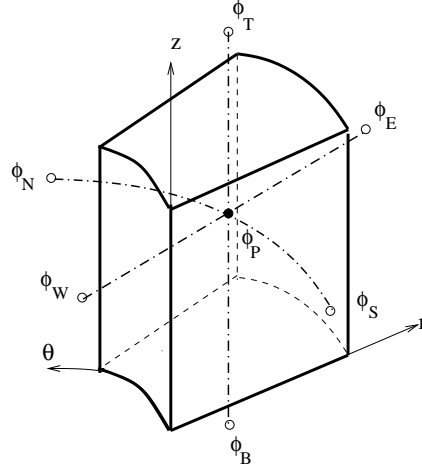
Figure 2.1: Location of nodal points at centred grid and its neighbours for cylindrical coordinate system (r, θ, z).

$$\int_{\Omega} \frac{\partial \phi}{\partial t} d\Omega + \int_{\Omega} \nabla \cdot \mathbf{J} d\Omega = \int_{\Omega} S_{\phi} d\Omega \tag{2.10}$$

Using the divergence theorem for the term $\int_{\Omega} \nabla \cdot \mathbf{J} d\Omega$ and approaching the right hand side term as the average source term of the whole control volume yields:

$$\int_{\Omega} \frac{\partial \phi}{\partial t} d\Omega + \int_{\partial \Omega} \mathbf{J} \cdot \mathbf{n} dS = \overline{S_{\phi}} \Omega \tag{2.11}$$

where $\partial \Omega$ is the outer surface of the CV of volume Ω, and $\mathbf{n}$ a unit vector normal to the surface. Expressing the integral term containing the flux vector in Eqn. 2.11 as a summation of the contribution on each face:

$$\int_{\Omega} \frac{\partial \phi}{\partial t} d\Omega + \sum_{f} J_f = \overline{S_{\phi}} \Omega \tag{2.12}$$

In Eqn. 2.12, J_f represents the integral flux of the variable ϕ across the face f (f = w,e,n,s,b,t). According with the representation in Fig. 2.1, e.g., e represents the interface between nodal points P and E. This integral flux J_f considers both, the

diffusive and the convective fluxes, of the variable ϕ at the face f with surface S_f. In order to integrate each term in the above equation, it is better to consider the diffusive flux (J_f^D) independently of the convective flux (J_f^C):

$$J_f = J_f^C + J_f^D \tag{2.13}$$

In order to explain the integration of the diffusive and convective fluxes, the fluxes at the face e will be used as an example.

Diffusive terms have been approximated using a piecewise-linear profile also known as second order central differences scheme:

$$
\begin{aligned}
J_e^D &= \int_e \mathbf{J^D} \cdot \mathbf{n} dS = \int_e -\Gamma \nabla \phi \cdot \mathbf{n} dS = \int_e -\Gamma \frac{\partial \phi}{\partial r} dS \approx \\
&- \Gamma_e \left(\frac{\partial \phi}{\partial r} \right)_e S_e \approx -\Gamma_e S_e \frac{\phi_P - \phi_E}{\delta r_e} = D_e(\phi_E - \phi_p)
\end{aligned}
\tag{2.14}
$$

In the above expression the value of the diffusion coefficient Γ_e is located at the interface of the control volumes (between neighbouring nodal points E and P). The mathematical formulation here presented considers thermophysical properties constants. However, care must be taken in the formulation of the interface between two different materials. The desired expression for Γ_e (at the interface) is the one that leads to the correct flux through the interface. That is, the flux that leaves one control volume through a particular face must be identical to the flux that enters the next control volume through the same face.

Convective terms have been approximated as:

$$J_e^C = \int_e \mathbf{J^C} \cdot \mathbf{n} dS = \int_e \mathbf{u} \phi \cdot \mathbf{n} dS = \int_e u_e \phi dS \approx u_e \phi_e S_e = F_e \phi_e \tag{2.15}$$

The critical point is the evaluation of the variable ϕ at the face of the control volume. To obtain accurate solutions avoiding convergence problems, different numerical schemes have been reviewed, such as the Upwind Differencing Scheme (UDS), the Quadratic Upstream Interpolation for Convective Kinematics (QUICK) [2], the second order accurate Upwind [3] or the SMART scheme [4]. The first and the last ones have been used along this thesis. For high order numerical schemes (such as SMART) the deferred correction approach procedure [5, 6] has been implemented. Thus, the convective flux at the interface has been evaluated as:

$$F_e \phi_e = F_e \phi_e^U - F_e(\phi_e^U - \phi_e^H) \tag{2.16}$$

where ϕ_e^U is the first order accurate UDS scheme and ϕ_e^H is the variable evaluated using a high order numerical scheme. In the UDS approximation, the value of ϕ at

the interface has been evaluated using the value of ϕ on the *upwind* side of the face, depending on the value of the flux F_e. Thus,

$$\phi_e^U = \begin{cases} \phi_P & \text{if } F_e > 0 \\ \phi_E & \text{if } F_e < 0 \end{cases} \tag{2.17}$$

The conditional statement can be compactly written in the following manner:

$$F_e \phi_e^U = \phi_P \max(F_e, 0) - \phi_E \max(-F_e, 0) \tag{2.18}$$

For the evaluation of ϕ_e^H, the SMART scheme has been used in this thesis. This scheme has a theoretical accuracy order between 1 and 3. The SMART scheme states that the value of the variable at the face depends on the value of the two nodal points upstream and the neighbour nodal point downstreams. That is:

$$\phi_e = f(\phi_u, \phi_c, \phi_d) \tag{2.19}$$

where ϕ_u, ϕ_c and ϕ_d depends on the flux direction. ϕ_u is the second nodal point upstream, ϕ_c is the neighbour nodal point upstream, while ϕ_d is the neighbour nodal point downstream. Then, depending on the flow direction:

$$\phi_u = \begin{cases} \phi_W & \text{if } F_e > 0 \\ \phi_{EE} & \text{if } F_e < 0 \end{cases} \tag{2.20}$$

$$\phi_c = \begin{cases} \phi_P & \text{if } F_e > 0 \\ \phi_E & \text{if } F_e < 0 \end{cases} \tag{2.21}$$

$$\phi_d = \begin{cases} \phi_E & \text{if } F_e > 0 \\ \phi_P & \text{if } F_e < 0 \end{cases} \tag{2.22}$$

In order to formulate in a compact manner the SMART scheme, it is better to work with the normalised variables. Thus,

$$\overline{\phi} = \frac{\phi - \phi_u}{\phi_d - \phi_u} \tag{2.23}$$

In a similar way, it is also convenient the introduction of the non-dimensional distances:

$$\overline{r} = \frac{r - r_u}{r_d - r_u} \tag{2.24}$$

40

With the above non-dimensional variables, the SMART scheme can be formulated as follows:

$$\bar{\phi}_e = \begin{cases} -\dfrac{\bar{r}_e(1 - 3\bar{r}_c + 2\bar{r}_e)}{\bar{r}_c(\bar{r}_c - 1)}\bar{\phi}_c & 0 < \bar{\phi}_c < \dfrac{\bar{r}_c}{3} \\[2em] \dfrac{\bar{r}_e(\bar{r}_e - \bar{r}_c)}{1 - \bar{r}_c} + \dfrac{\bar{r}_e(\bar{r}_e - 1)}{\bar{r}_c(\bar{r}_c - 1)}\bar{\phi}_c & \dfrac{\bar{r}_c}{3} < \bar{\phi}_c < \dfrac{\bar{r}_c}{\bar{r}_e(1 + \bar{r}_e - \bar{r}_c)} \\[2em] 1 & \bar{\phi}_c < \dfrac{\bar{r}_c}{\bar{r}_e(1 + \bar{r}_e - \bar{r}_c)} < 1 \\[2em] \bar{\phi}_c & \text{otherwise} \end{cases} \qquad (2.25)$$

For the integration of the **transient term**, $\partial\phi/\partial t$, it is assumed that the value of ϕ at the centre of the grid volume prevails throughout the control volume. Then,

$$\int\limits_{\Omega} \int\limits_{t}^{t+\Delta t} \frac{\partial\phi}{\partial t}d\Omega \approx \frac{(\phi_P - \phi_P^0)}{\Delta t}\Omega_P \qquad (2.26)$$

where ϕ_P is the value of the variable at the current time step and ϕ_P^0 is the value of the variable at the last time step.

For the **source term** it is also assumed that the value of the nodal point prevails over all the control volume:

$$\overline{S_\phi} = S_P \qquad (2.27)$$

Combining all the previous expressions, the discretised *convection-diffusion* equation can be written as:

$$\begin{aligned} \frac{(\phi_P - \phi_P^0)}{\Delta t}\Omega_P &+ (J_e^D + F_e\phi_e^U) - (J_w^D + F_w\phi_w^U) + (J_n^D + F_n\phi_n^U) \qquad (2.28) \\ &- (J_s^D + F_s\phi_s^U) + (J_t^D + F_t\phi_t^U) - (J_b^D + F_b\phi_b^U) \\ &= S_P\Omega_P + b_{de} \end{aligned}$$

In Eqn. 2.28, the term b_{de} is the deferred correction approach term to achieve the high order accuracy precision. This correction has been done by evaluating the values of the variable at the faces according to the currently available nodal values,

$$\begin{aligned} b_{de} &= F_e(\phi_e^U - \phi_e^H) - F_w(\phi_w^U - \phi_w^H) \qquad (2.29) \\ &+ F_n(\phi_n^U - \phi_n^H) - F_s(\phi_s^U - \phi_s^H) \\ &+ F_t(\phi_t^U - \phi_t^H) - F_b(\phi_b^U - \phi_b^H) \end{aligned}$$

Thus, rearranging Eqns. 2.28 and 2.29, the algebraic equations have the following structure:

$$a_P \phi_P = \sum_{nb} a_{nb} \phi_{nb} + b \qquad (2.30)$$

where the subscript nb takes the value of the neighbouring points ($nb = W$, E, S, N, B, T). These coefficients can be evaluated as:

$$
\begin{aligned}
a_E &= D_e + \max(-F_e, 0) && (2.31) \\
a_W &= D_w + \max(F_w, 0) \\
a_N &= D_n + \max(-F_n, 0) \\
a_S &= D_s + \max(F_s, 0) \\
a_T &= D_t + \max(-F_t, 0) \\
a_B &= D_b + \max(F_b, 0) \\
a_P &= \sum_{nb} a_{nb} + F_e - F_w + F_n - F_s + F_t - F_b + \frac{\Omega_P}{\Delta t} \\
b &= S_P \Omega_P + \phi_P^0 \frac{\Omega_P}{\Delta t} + b_{de}
\end{aligned}
$$

The integration of the *convection-diffusion* equation for all control volumes in the domain, leads to an algebraic system of equations for a single variable ϕ. The above discretisation can be applied for the momentum equations at each direction and for the energy equation. Mass conservation equation deserves a special attention, which is explained in the next subsection.

The algebraic system of linear equations resulting for each variable have been solved in the present work using a Multigrid method [7]. Multigrid methods are highly efficient techniques for solving the algebraic set of equations. The basic idea is to use multiple grids to resolve different error frecuencies of the solution on the appropriate scale. Classic iterative solvers such as MSIP or line-by-line Gauss-Seidel degrade with the increase of the mesh to be solved. However, these iterative solvers are efficient reducing high frequency errors. Thus, multigrid methods converts low frequency errors on the fine grid to high frequency errors on the coarse grid, that can be dealt with iterative solvers. The overall convergence rate is greatly increased in this way.

2.3.1 The pressure correction equation. The SIMPLE-like algorithm

In momentum equation for the radial, azimuthal and axial directions, the source term S_P in the coefficient b, contains the pressure gradient, the temperature effects

over the density (i.e. the Boussinesq's hypothesis), and the term derived from the cylindrical coordinate system on their respective directions. Thus, for the resulting systems of equations it is said to have a coupling between the velocities (i.e. v_r, v_θ and, v_z), the temperature T, and the pressure p.

In order to solve the velocities components, i.e. the momentum equations in each direction, a pressure field must to be guessed. Denoting the velocity field obtained from a guessed pressure field as, e.g. for axial direction, v_z^*:

$$a_n v_{z,t}^* = \sum_{nb} a_{nb} v_{z,nb}^* + b_z + (p_P^* - p_T^*)S_t \tag{2.32}$$

In the above equation, the coefficient b_z is defined in the same manner as in Eqn. 2.31, but the pressure gradient has not been included. Notice that velocity and pressure have been denoted as v_z^* and p^*. The velocities evaluated with the above expression, satisfy only the momentum conservation. There is no guarantee about continuity, unless the correct pressure field is employed. Thus, the objective is to find a pressure field that satisfy continuity equation. Correcting the guessed p^* value, is obtained:

$$p = p^* + p' \tag{2.33}$$

Here, p' is called the pressure correction. Introducing the same corrections for the velocities, in a similar manner, we can write the velocity fields as a function of the pressure correction, such as:

$$v_z = v_z^* + v_z' \tag{2.34}$$

The same applies for the velocities at the radial and azimuthal directions. Substituting these expressions in the algebraic system of equations for the continuity equation is obtained:

$$a_t v_{z,t}' = \sum_{nb} a_{nb} v_{znb}' + (p_P' - p_T')S_t \tag{2.35}$$

In this point different approaches can be considered. One of these, neglects the summation term in Eqn. 2.35. This approach is known as the SIMPLE approach (Semi-Implicit Method for Pressure-Linked Equations) giving,

$$v_{z,t}' = (p_P' - p_T')d_t \tag{2.36}$$

where $d_t = S_t/a_t$. Another possibility, is an improvement of the approach proposed above, which considers also the neighbour summation. This approach is called SIMPLEC (Semi-Implicit Method for Pressure-Linked Equations Consistent) [8]. Thus, d_t is written as:

$$d_t = \frac{S_t}{a_t - \sum\limits_{nb} a_{nb}} \tag{2.37}$$

The Eqn. 2.35 is the velocity correction formula. Substituting this expression in Eqn. 2.34, velocity can be written as:

$$v_z = v_z^* + d_t(p_P' - p_T') \tag{2.38}$$

The last approach has been adopted in the present thesis. To evaluate the pressure correction, the mass conservation equation has been written properly to formulate an equation for the pressure correction. Integrating the continuity equation over a control volume and assuming that density, ρ_P, prevail over all control volume, and that velocity components (v_r, v_θ, and v_z) are placed at the faces of the control volume, the integrated equation reads,

$$
\begin{aligned}
& [(\rho v_r)_e - (\rho v_r)_w]r\Delta\theta\Delta z \\
+ \ & [(\rho v_\theta)_n - (\rho v_\theta)_s]\Delta r\Delta z \\
+ \ & [(\rho v_t)_n - (\rho v_z)_b]r\Delta r\Delta\theta = 0
\end{aligned}
\tag{2.39}
$$

Substituting the velocity components by the velocity correction formulae (such as Eqn. 2.38), and rearranging terms, a discretisation equation for pressure correction can be obtained:

$$a_P p_P' = a_E p_E' + a_W p_W' + a_N p_N' + a_S p_S' + a_T p_T' + a_B p_B' + b \tag{2.40}$$

where

$$
\begin{aligned}
a_E \ &= \ \rho_e d_e r\Delta\theta\Delta z \\
a_W \ &= \ \rho_w d_w r\Delta\theta\Delta z \\
a_N \ &= \ \rho_n d_n \Delta r\Delta z \\
a_S \ &= \ \rho_s d_s \Delta r\Delta z \\
a_T \ &= \ \rho_t d_t r\Delta r\Delta\theta \\
a_B \ &= \ \rho_b d_b r\Delta r\Delta\theta \\
a_P \ &= \ \sum_{nb} a_{nb} \\
b \ &= \ [(\rho v_r^*)_e - (\rho v_r^*)_w]r\Delta\theta\Delta z \\
&\quad + \ [(\rho v_\theta^*)_n - (\rho v_\theta^*)_s]\Delta r\Delta z + [(\rho v_z^*)_t - (\rho v_z^*)_b]r\Delta r\Delta\theta
\end{aligned}
\tag{2.41}
$$

It can be observed that if the coefficient b is zero, the values of the guessed velocities (v^*) in conjuction with the values of the density, satisfy the continuity equation, and no pressure correction is needed.

To solve the coupling between the equations, first, the system of equations for the velocities (equation of motion in r, θ and z directions) with the assumption of a pressure $p*$ and a temperature T fields can be solved. Then, with the velocity field from the previous step, the resolution of the pressure correction system of equations is done and p' is obtained. Once p' has been calculated, velocity and pressure fields are corrected and thus, the energy equation is solved. Following this iterative procedure it is possible to uncouple the system of equations. This iterative procedure, that solves the algebraic system of equations in a segregate manner, has been summarised in the so-called SIMPLE-like algorithm. This algorithm treat the coupling between pressure and velocity by means of the pressure correction equation commented above. The procedure can be summarised as follows:

1. Guess the pressure field $p*$

2. Solve momentum equations to obtain v_r*, $v_\theta*$ and v_z*

3. Solve the p' equation

4. Correct pressure and velocity fields to obtain p, v_r, v_θ and v_z by means of Eqns. 2.36 and 2.38

5. Solve the equation for temperature T

6. Treat corrected pressure p as a new guessed $p*$ and return to step 2 until convergence is reached.

2.3.2   The time marching algorithm

The SIMPLE-like algorithm commented above, allow to evaluate the values of the variables at a given time instant, from the conditions of the previous time step, $t - \Delta t$, (see temporal discretisation). Time marching can be used in different ways: to obtain a time solution of a transient flow or to obtain a steady-state solution by solving the evolution of the variables in time until steady-state is reached. In the last situation, this way of solving the system is called pseudo-transient method. In the case of a pseudo-transient problem, the solution at each time step must not to be time-accurate, advancing in time until the steady state is reached.

The resolution of the governing equations in time has been carried out by solving iteratively all variables at a given time instant. If the problem to be solved is transient, convergence of the iterative algorithm must to be reached at each time step,

advancing in time until the criteria to stop simulation is obtained (usually a given time).

For transient flow, the time step is limited by the truncation error associated with the discretisation of the time derivatives. In the present thesis, the transient term has been approximated by a first order time derivative. In order to model the transient phenomena properly, it is necessary to set Δt at least one order of magnitude smaller that the smallest time constant in the system to being modeled. A good way to judge, *a priori*, if a properly Δt has been chosen is, to observe the number of outer iterations per time step that the iterative algorithm used needs. If the number of outer iterations is greater than 20-30, the time step is probably, too large. Sometimes, the first time increments needs a large number of iteraterations to converge. Thus, a smaller Δt can be chosen for the first time steps and then this value can be increased as the time advances.

2.3.3 Particularities of the discretisation in cylindrical coordinates

The main particularities of the discretised set of PDEs in cylindrical coordinates, are the singularity that results at the cylinder centre ($r = 0$) and the spatial periodicity that appears in the azimuthal direction for closed geometries. Hereafter, a brief explanation of these particularities and the treatment carried out to overcome them are given.

A note on the treatment the singularity at the cylinder centre

On the discretisation of the governing equations at the axis, when the cylinder centre is within the computational domain, terms like ($1/r \ \partial\phi/\partial r$) or like ($\partial\phi/\partial\theta$) become undefined causing a singularity at the cylinder centre ($r = 0$). In order to circumvent these difficulties, different numerical strategies for the definition of boundary conditions at the cylinder axis have been proposed in the literature.

De Vahl Davis [9] suggested a discretisation without nodes at the centre of the cylinder. This means that the computational domain contains a thin cylinder around the z-axis. Radial derivatives of the innermost nodal points have been approximated by a second order forward difference formula. Schneider and Straub [10] proposed to introduce a cylinder-shape control volume at the axis and radial velocities at points on the radial face of the control volume have been then calculated. Another method for dealing with the axis of a cylindrical grid is to employ a mixed Cartesian and cylindrical grid system (i.e. use a Cartesian grid system at the region near the axis of the cylinder, and a cylindrical grid away the centre).

A different strategy has been proposed by Hiroyuki et al. [11]. In their work, they have evaluated radial velocity components at the centre for each θ angle of the
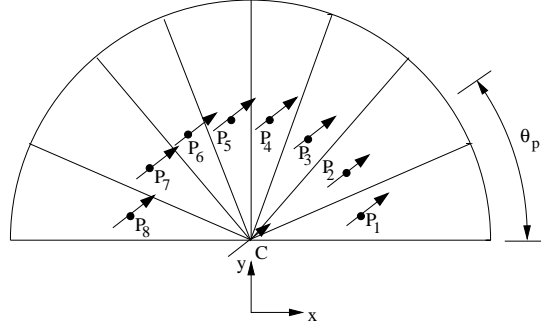
Figure 2.2: Discretisation at the centre of the cylinder. Axis node and its neighbours nodes.

azimuthal discretisation (i.e. $r = 0, \theta$), as a interpolation of the azimuthal velocity at the adjacent nodes in $\theta \pm \pi/2$ (i.e. $r = \Delta r, \theta \pm \pi/2$). A similar interpolation has been used for the azimuthal velocity component at the centre, but in this case, the interpolation has been done with the azimuthal velocities at the adjacent nodes at $\theta \pm \pi$ (i.e. $r = \Delta r, \theta \pm \pi/2$). For scalar variables, values at the axis have been obtained by averaging the values at the adjacent nodes.

Previous experiences at CTTC about the treatment of the singularity at the axis have been reported in the PhD thesis of A. Ivancic [12]. In his work, an additional control volume for momentum equation in radial direction to ensure information about v_r was introduced. After that, different cases were solved in order to verify this approach. However, in the present thesis, a different approach has been adopted.

In the approach adopted, no additional or 'special' control volumes at the centre are required. Once the grid has been generated, the values of the different variables have been prescribed at the centre as a boundary condition. To do so, first of all, Cartesian velocity components at the nearest nodes to the centre have been determined (see Fig. 2.2).

$$\vec{v}_{pi} = v_{x,pi}\vec{i} + v_{y,pi}\vec{j} + v_{z,pi}\vec{k} \qquad i = 1, 2, 3... \qquad (2.42)$$

where,

$$
\begin{aligned}
v_{x,pi} &= v_{r,pi}\cos\theta_{pi} - v_{\theta,pi}\sin\theta_{pi} & (2.43)\\
v_{y,pi} &= v_{r,pi}\sin\theta_{pi} + v_{\theta,pi}\cos\theta_{pi} & (2.44)\\
v_{z,pi} &= v_{z,pi} & (2.45)
\end{aligned}
$$

47

Velocity vector at the cylinder centre ($\vec{v}_c$) has been then calculated as the average value of the Cartesian components of velocity at the nearest nodes ($\vec{v}_{pi}$).

$$\vec{v}_c = v_{x,c}\vec{i} + v_{y,c}\vec{j} + v_{z,c}\vec{k} \tag{2.46}$$

$$v_{x,c} = \sum_{i=1}^{N\theta} v_{x,pi}\Delta\theta_{pi}/2\pi \tag{2.47}$$

$$v_{y,c} = \sum_{i=1}^{N\theta} v_{y,pi}\Delta\theta_{pi}/2\pi \tag{2.48}$$

$$v_{z,c} = \sum_{i=1}^{N\theta} v_{z,pi}\Delta\theta_{pi}/2\pi \tag{2.49}$$

Once the velocity components of the vector at the cylinder centre have been obtained, their values can be written for cylindrical coordinates as:

$$
\begin{aligned}
v_{r,c} &= v_{x,c}\cos\theta_c + v_{y,c}\sin\theta_c \\
v_{\theta,c} &= -v_{x,c}\sin\theta_c + v_{y,c}\cos\theta_c \\
v_{z,c} &= v_{z,c}
\end{aligned}
\tag{2.50}
$$

The values of the velocity components at each θ angle is introduced as boundary conditions of the momentum equations at each direction (radial, axial and azimuthal).

The discretisation at the centre proposed, overcomes in a simpler manner the main difficulties of the different approaches found in literature (i.e. no additional or special CV's are necessary; different values of the velocity vector at the centre, depending of the θ angle considered; use of Cartesian and cylindrical grids at different zones of the domain; among others). The main advantage is that only one velocity vector is calculated at the centre of the cylinder, being the components of the velocity at each discretisation angle θ evaluated from this vector. The appropriateness of this approach is discussed in the next chapter.

A note on periodic boundary conditions

In three-dimensional cylindrical coordinate systems, when there are no boundaries in the azimuthal direction (i.e. cylindrical domains), the domain is considered spatially periodic. From the numerical integration of the governing differential equations over the discretised domain, the resulting set of the algebraic system of equations is characterised for having a cyclic heptadiagonal coefficient matrix that is usually solved with specific algorithms [13, 14, 15]. An alternative to this methodology

is the discretisation of the domain introducing a false boundary at the azimuthal direction and conveniently formulating a spatially periodic boundary condition. This is the strategy that has been followed in this thesis. A brief explanation is hereafter presented.

Once the domain has been discretised, four control volumes have been added at the outer boundary in the azimuthal direction ($\theta = 2\pi$). These supplementary control volumes have been overlapped onto the corresponding ones at the inner domain boundary ($\theta = 0$).

The way the information has been transferred between the overlapped nodes is schematically represented in Fig. 2.3. In the figure, $N\theta$ corresponds to the total number of nodal points in the azimuthal direction for the centred grid, once the four CV's have been added. Considering the staggered location of the velocity components, two treatments can be distinguished: one for scalar variables p_d and T and velocity components v_r and v_z (Fig. 2.3a) and a different one for the azimuthal velocity v_θ (Fig. 2.3b). Taking into account the array indexation presented in Fig. 2.3, the spatial boundary condition in the azimuthal direction can be summarised as follows:

> From the two innermost control volumes of the overlapping zone (corresponding to $j = 3, 4, N\theta - 4, N\theta - 5$), the values of the variables v_r, v_z, T and p_d are directly transferred to the corresponding overlapped nodes:
>
> $$\begin{aligned}
> \phi(i,1,k) &= \phi(i,2,k) & \phi(i,N\theta - 2,k) &= \phi(i,4,k) \\
> \phi(i,2,k) &= \phi(i,N\theta - 4,k) & \phi(i,N\theta - 1,k) &= \phi(i,5,k) \\
> \phi(i,3,k) &= \phi(i,N\theta - 3,k) & \phi(i,N\theta,k) &= \phi(i,N\theta - 1,k)
> \end{aligned} \tag{2.51}$$
>
> For the particular case of v_θ, in the staggered mesh in azimuthal direction, the transfer information is given by:
>
> $$\begin{aligned}
> \phi(i,1,k) &= \phi(i,N\theta - 5,k) & \phi(i,N\theta - 1,k) &= \phi(i,5,k) \\
> \phi(i,2,k) &= \phi(i,N\theta - 4,k) & \phi(i,N\theta - 2,k) &= \phi(i,4,k)
> \end{aligned} \tag{2.52}$$

This strategy assesses that the numerical solution obtained from the integration of the governing equations is the same as the one that could be obtained without the definition of this spatially periodic boundary condition. In this sense, the number of control volumes considered to define the overlapping zone has been selected in order to maintain the order of accuracy of the numerical solutions when convective terms are evaluated using third order numerical schemes.
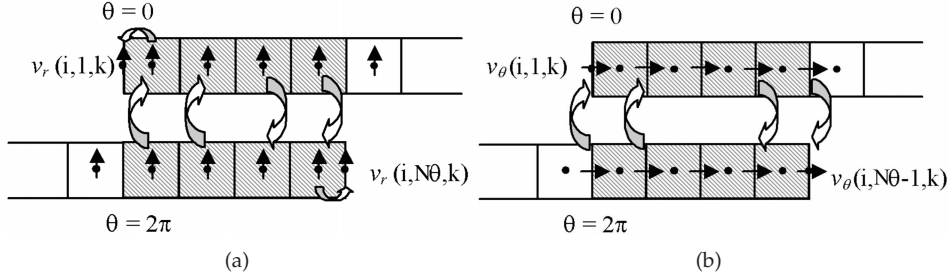
Figure 2.3: Treatment of radial and azimuthal velocity components in the periodic zone. (a) Radial velocity component. (b) Azimuthal velocity component.

2.4 Verification of the code and numerical solutions (V&V)

As computational fluid dynamics is fast becoming a tool in the engineering design process, the numerical uncertainty assessment is necessary to make solutions reliable. Many papers have been published concerning the quantification of errors and uncertainties in CFD simulations [16, 17, 18, 19, 20, 21]. Adopting the semantics proposed by Roache [22], two main concepts can be distinguished: the verification of the code and the verification of the numerical solutions. Code verification is referred to the identification of programming errors, while verification of the numerical solutions accounts for the quantification of the remaining sources of computational errors, mainly corresponding to the discretisation errors.

In the process of code verification and verification of calculations, the post-processing procedure proposed by Cadafalch et al.[23] has been used. This post-processing tool is based on the generalised Richardson extrapolation for *h-refinement* studies and on the Grid Convergence Index (*GCI*) proposed by Roache [16]. A brief description of this procedure is given below. For more details see [23].

2.4.1 Concepts and definitions

Richardson extrapolations method states that the error in a numerical solution can be expressed as [24, 25]:

$$e_D(\mathbf{x}) = \phi_0(\mathbf{x}) - \phi(\mathbf{x}) = \alpha_1 h + \alpha_2 h^2 + \alpha_3 h^3 + ...$$ (2.53)

where $\phi_0(\mathbf{x})$ is the exact numerical solution and $\phi(\mathbf{x})$ is the numerical solution ob-

tained with a grid size h and, α_i ($i = 1, 2, 3..$), are coefficients which can be function of the coordinates but independent on h in the asymptotic range. For a sufficiently small value of h (i.e. when $h \to 0$), the local discretisation error, $e_D(\mathbf{x})$, can be approximated in terms of the numerical solution $\phi(\mathbf{x})$ obtained with the mesh spacing h, and the leading term of the truncation error as:

$$e_D(\mathbf{x}) = \phi_0(\mathbf{x}) - \phi(\mathbf{x}) = C(ah)^{p(\mathbf{x})} \tag{2.54}$$

where $p(\mathbf{x})$ is the order of the numerical scheme used, C is a coefficient independent of h but can be function of the space or time and, a that is the mesh ratio [18]. Richardson extrapolation uses calculations on multiple set of grids. The grid size of each solution can be expressed as a function of the grid size of the finest one ($h_1 = h_{ref}$) as:

$$h_i = a_i h_{ref} \qquad\qquad i = 1, 2, 3, .. \tag{2.55}$$

where the subscript $i = 1$ represents the finest grid. Expression 2.54 can be written for each grid solution (p.e. for three grid solutions) giving a set of equations:

$$\phi_0(\mathbf{x}) - \phi_1(\mathbf{x}) = C_p(a_1 h)^{p(\mathbf{x})} \tag{2.56}$$
$$\phi_0(\mathbf{x}) - \phi_2(\mathbf{x}) = C_p(a_2 h)^{p(\mathbf{x})}$$
$$\phi_0(\mathbf{x}) - \phi_3(\mathbf{x}) = C_p(a_3 h)^{p(\mathbf{x})}$$

being $a_1 = 1$, the above system of equations (Eqn. 2.56) can be solved for the three grids and the values for p, c_p and $\phi_0(\mathbf{x})$ can be obtained . The solution of the above system of equations gives:

$$p(\mathbf{x}) = \frac{\ln[(\phi_2(\mathbf{x}) - \phi_3(\mathbf{x}))/(\phi_1(\mathbf{x}) - \phi_2(\mathbf{x}))]}{\ln a_2} - f(p) \tag{2.57}$$

$$f(p) = \frac{\ln[((a_3/a_2)^{p(\mathbf{x})} - 1)/(a_2^{p(\mathbf{x})} - 1)]}{\ln(a_2)} \tag{2.58}$$

$$\phi_0(\mathbf{x}) = \frac{a_2^{p(\mathbf{x})} \phi_1(\mathbf{x}) - \phi_2(\mathbf{x})}{a_2^{p(\mathbf{x})} - 1} \tag{2.59}$$

For a constant grid refinement ratio (i.e. $a_3/a_2 = a_2 = r$), Eqn. 2.58 equals zero and Eqn. 2.57 can be solved directly. Otherwise Eqns. 2.57 to 2.59 need to be solved iteratively. Thus, substituting Eqn. 2.59 into Eqn. 2.54 for the finest grid, gives:

$$e_D(\mathbf{x}) = \left| \frac{\phi_1(\mathbf{x}) - \phi_2(\mathbf{x})}{r^{p(\mathbf{x})} - 1} \right| \tag{2.60}$$

Roache [16] incorporates a safety factor F_s and define the **Grid Convergence
Index** (GCI) for the fine grid solution as:

$$GCI(\mathbf{x}) = F_s \left| \frac{\phi_1(\mathbf{x}) - \phi_2(\mathbf{x})}{r^{p(\mathbf{x})} - 1} \right| \qquad (2.61)$$

The value of the safety factor must be taken depending on the number of grid
solutions available. For two grid solutions, a conservative value of $F_s = 3$ is recom-
mended, while for three or more grids solutions $F_s = 1.25$ seems to be adequate.
The calculation of the order of accuracy and the GCI by Eqns. 2.57 and 2.61 implies
that the solutions of the three set of grids have monotonic convergence to the exact
numerical solution as the grid is refined. That is, the ratio $(\phi_2(\mathbf{x}) - \phi_3(\mathbf{x}))/(\phi_1(\mathbf{x}) - \phi_2(\mathbf{x})) > 0$. Richardson extrapolations for cases with oscillatory convergence needs
further investigations and is beyond the scope of this thesis [18, 21].

2.4.2 Post-processing tool

The post-processing procedure implemented by Cadafalch et al. [23] processes the
numerical solutions for all variables of the problem, obtained from three consecu-
tive levels of discretisation in an *h-refinement* study with a constant mesh ratio of
$r = 2$. The value of the mesh ratio is fixed in Eqn. 2.57 by doing $a_2 = r = 2$.
Other *h-refinement* ratios could be considered, just changing this value in Eqn. 2.57,
but always maintaining constant the mesh ratio (Eqn. 2.58 equals zero). Numeri-
cal solutions are interpolated at the post-processing grid. The post-processing grid
is assigned to the coarsest one of the three levels of refinement considered. In or-
der to minimise the introduction of errors during interpolation, third order accurate
Lagrangian interpolations are used.

The most relevant parameters arisen from this procedure are the uncertainty due
to the discretisation (GCI), the observed order of accuracy of the numerical solution
(p), and the percentage of nodes where the application of the post-processing pro-
cedure has been possible (called Richardson nodes ($Rn[\%]$)). Richardson nodes are
those where $(\phi_2(\mathbf{x}) - \phi_3(\mathbf{x}))/(\phi_1(\mathbf{x}) - \phi_2(\mathbf{x})) > 0$.

Global and local estimators of the GCI and p are obtained for the finest mesh and
for each dependent variable of the problem. Global estimates, especially useful for
reporting results of the verification process in a compact manner, are evaluated by
means of a volume weighted average. In order to evaluate the GCI (Eqn. 2.61) the
value of the order of accuracy introduced in the formula is the global observed order
of accuracy of the solution. For the GCI evaluation, a safety factor of $F_s = 1.25$ is
taken.

It has been shown in previous works [23, 26] that GCI estimates are credible
when the global observed order of accuracy (p) for each variable approaches its the-

52

oretical value (e.g. 2, in second order differencing schemes), and when the number of the Richardson nodes is high enough. In this thesis, local and global estimators have also been useful in order to find out the appropriate grid parameters such as determine the zones where the discretisation mesh requires additional refinement, as is further commented.

2.5 Conclusions

The governing equations for the resolution of heat transfer and fluid flow in three-dimensional cylindrical coordinates have been presented. A detailed description of the discretisation employed on the development of a CFD and heat transfer code has been exposed. Special emphasis has been done on the singularity treatment at the cylinder centre and on the spatial periodicity at the azimuthal direction. The post-processing procedure followed in the assessment of the numerical solutions, in order to quantify errors and uncertainties, has been also exposed.

Nomenclature

c_p	specific heat (J/kgK)	Rn	Richardson nodes (%)
e_D	exact global discretisation error (%)	T	temperature (K)
GCI	Grid Convergence Index (%)	t	time (s)
g	acceleration of gravity (m/s^2)	$N\theta$	total number of nodes in the azimuthal direction
k	thermal conductivity (W/mK)	u	magnitude of velocity vector (m/s)
p_d	dynamic pressure (Pa)	v_r	radial velocity component (m/s)
p	observed order of accuracy	v_θ	azimuthal velocity component (m/s)
$\dot{q}$	heat flux (W/m^2)	v_z	axial velocity component (m/s)
r	radial coordinate (m)	z	axial coordinate (m)

Greeks

α	thermal diffusivity (m^2/s)	ν	kinematic viscosity (m^2/s)
β	thermal expansion coefficient (K^{-1})	θ	azimuthal coordinate (rad)
ϕ	dependent variable	ρ	density (kg/m^3)
μ	dynamic viscosity (kg/ms)	τ	stress tensor (N/m^2)

References

[1] S.V. Patankar. *Numerical heat transfer and fluid flow*. Hemisphere Publishing Corporation, 1980.

[2] B.P. Leonard. A stable and accurate convective modelling procedure based on quadratic upstream interpolation. *Computer Methods in Applied Mechanics and Engineering*, 19:59–98, 1979.

[3] Shyy W. A study of finite difference approximations to steady state convection dominated flow problems. *Journal of Computations in Physics*, 57:415–438, 1985.

[4] P.H. Gaskell and A.K.C. Lau. Curvature-compensed convective transport: SMART, a new boundedness-preserving transport algorithm. *International Journal for Numerical Methods in Fluids*, 8:617–641, 1988.

[5] M.S. Darwish. A new high-resolution scheme based on the normalized variable formulation. *Numerical Heat Transfer, Part B*, 30(24):353–371, 1993.

[6] M.S. Darwish and F. Moukalled. Normalized variable and space formulation methodology for high-resolution schemes. *Numerical Heat Transfer, Part B*, 26:79–96, 1994.

[7] B.R. Hutchinson and G.D.Raithby. A multigrid method based on the additive correction strategy. *Numerical Heat Transfer, Part B*, 9:511–537, 1986.

[8] J.P. Van Doormal and G.D. Raithby. Enhancements of the simple method for predicting incompressible fluid flows. *Numerical Heat Transfer*, 7:147–163, 1984.

[9] G. De Vahl Davis. A note on a mesh for use with polar coordinates. *Numerical Heat Transfer*, 2:261–266, 1979.

[10] S. Schneider and J. Straub. Laminar natural convection in a cylindrical enclosure with different end temperature. *International Journal of Heat and Mass Transfer*, 35(2):545–557, 1992.

[11] O. Hiroyuki and T. Keiji. A technique to circumvent a singularity at a radial center with application for a three-dimensional cylindrical system. *Numerical Heat Transfer, Part B*, 33:355–365, 1998.

[12] A. Ivancic. *Simulación numérica de la convección natural y forzada en recintos cilíndricos. Aplicación a la acumulación de calor y frío*. PhD thesis, Universitat Politècnica de Catalunya, 1998.

References

[13] I. M. Navon. Pent: a periodic pentadiagonal systems solver. *Communications in Applied Numerical Methods*, 3:63–69, 1987.

[14] S. Sebben and B. Rabi Baliga. Some extensions of tridiagonal and pentadiagonal matrix algorithms. *Numerical Heat Transfer, Part B*, 28:323–351, 1996.

[15] X. Sun and S. Moitra. Performance comparison of a set of periodic and non-periodic tridiagonal solvers on SP2 and Paragon Parallel Computers. *Concurrency: Practice and experience*, 9(8):781–801, 1997.

[16] P.J. Roache. Perspective: a method for uniform reporting of grid refinement studies. *Journal of Fluids Engineering*, 116:405–413, 1994.

[17] I. Celik and Vei-Ming Zhang. Calculation of numerical uncertainty using richardson extrapolation: application to some simple turbulent flow calculations. *Journal of Fluids Engineering*, 117:439–445, 1995.

[18] I. Celik and O. Karatekin. Numerical experiments on application of Richardson extrapolation with non-uniform grids. *Journal of Fluids Engineering*, 119:584–590, 1997.

[19] AIAA guide for the verification and validation of computational fluid dynamics simulations, 1998.

[20] Stern F., Wilson R.V., Coleman H.W., and Paterson E.G. Comprehensive approach to verification and validations of CFD simulations- Part 1: Methodology and procedures. *Journal of Fluids Engineering*, 123:793–801, 2001.

[21] I. Celik, Jung Li, Gusheng Hu, and C. Shaffer. Limitations of Richardson extrapolations and some possible remedies. *Journal of Fluids Engineering*, 127:795–805, 2005.

[22] P.J. Roache. Code verification by the method of manufactured solutions. *Journal of Fluids Engineering*, 124:4–10, 2002.

[23] J. Cadafalch, C.D. Pérez-Segarra, R. Cònsul, and A. Oliva. Verification of finite volume computations on steady state fluid flow and heat transfer. *Journal of Fluids Engineering*, 124:11–21, 2002.

[24] Richardson L.F. The approximate arithmetical solution by finite differences of physical problems involving differential equations, withan application to the stresses in a mansonry dam. *Transactions of the Royal Society of London, Series A*.

[25] Roache P.J. *Verification and Validation in Computational Science and Engineering*. Hermosa Publisher, 1998.

[26] R. Cònsul, C.D. Pérez-Segarra, K. Claramunt, J. Cadafalch, and A. Oliva. Detailed numerical simulation of laminar flames by a parallel multiblock algorithm using loosely coupled computers. *Combustion Theory and Modelling*, 7(3):525–544, 2003.

Chapter 3

Verification of the code and verified numerical results on cylindrical coordinates

Abstract. In this chapter the tasks carried out in order to verify the code and the numerical solutions are presented. Different cases are submitted to a process of verification of the numerical solutions. The appropriateness of the adopted discretisation and the verification procedure are discussed analysing two problems with analytical solution: a uniform flow through a cylindrical domain and a laminar Couette flow. Verified computations for two and three-dimensional steady-state problems in cylindrical coordinates are provided: a flow induced by a tangential velocity at the boundary; a natural convection in a cylindrical enclosure heated from below, and the fluid motion between two concentric rotating cylinders. The most relevant results for velocity and temperature fields, together with their uncertainty estimates of the discretisation are given.

3.1   Introduction

The most important aspects in the verification of the code and numerical solutions during the process of a code development have been analised in the present chapter. The numerical solutions of different test cases in cylindrical coordinates have been submitted to a rigorous process of verification applying the techniques described in Chapter 2.

In the process of development or improvement of a CFD code there are several aspects to be taken into account. Once a mathematical model (governing equations) is considered in the modelisation of a given physical phenomena, the main job of a CFD code developer is to convert the set of partial differential equations (PDEs) to algebraic equations and to solve them using a computer. This conversion involves the discretisation of the PDEs, the programming of the code, the numerical algorithm, the criteria for finishing the convergence procedure, and the computer accuracy. Once this process is finished, it is important to submit the code and the calculations to a process of verification [1].

In the process of code verification the main job is to find programming bugs or mistakes that could have been introduced in its development. The common strategy is to submit the code to different kind of tests for which their solution is known. The nature of those tests can be diverse. The most desirable ones are those for which an analytical solution of the set of PDEs is known. However, the main inconvenient inherent of these tests is, that analytical solutions can be found mainly when quadratic terms become null, being not the most useful ones to exercise all terms of the set of PDEs. Another group of problems are those that although they do not have an analytical solution, they have been widely treated in the literature and are specially relevant to industrial and technical applications. An illustrative well known example of these kind of problems, usually defined as *benchmarks*, is the case proposed by Jones [2] consisting in a buoyancy-driven flow in a square cavity with differentially heated walls. De Vahl Davis [3, 4] summarised the results obtained by different research groups, and a *benchmark* solution was accepted. These solutions are nowadays being widely employed with the same level of confidence that an analytical solution may have. The third possible strategy that has been proposed recently consists in the obtention of an analytical solution by means of the Method of Manufactured Solutions (MMS) [5, 6, 7]. This method consists in the generation of an exact solution of some PDEs constructed by solving the problem *backwards*. This means that first, a preferable solution that exercises all terms in differential equations is chosen, and after that this solution is passed through the set of PDEs to find the source terms that satisfies them. The constructed solution does not necessarily correspond to a physical problem but concerns to a mathematical exercise.

Once a given problem is selected to verify the code, its numerical solution has to converge to the analytical or reference solution as the computational errors are re-

duced. These errors can be due to the convergence criteria, the accuracy of the computer, the geometrical and numerical discretisation, and to the presence of possible bugs or mistakes. If the first three causes are minimised, the remaining computational error is caused by programme mistakes that have to be detected.

Once the code is verified, it is ready to be employed on the numerical simulation of CFD and Heat Transfer phenomena. However, numerical solutions have to be verified. If the computer accuracy and convergence criteria are good enough, the remaining sources of computational errors are mainly due to the discretisation errors. Different strategies have been proposed to estimate the errors, such as those proposed by Roache [8], Becker and Rannacher [9], and Cadafalch et al. [10].

On the process of code verification of three-dimensional cylindrical coordinates CFD codes, there is a certain difficulty to find reference solutions in the literature to be employed in this task. Analytical solutions such as the Hagen-Poiseuille flow, the steady circular Couette flow [11, 12] and the uniform flow through a cylindrical domain can be mentioned. *Benchmark* problems that can be found in the literature are mainly for two or three-dimensional problems in rectangular domains and only a few of these are available for cylindrical geometries [13, 3, 14]. One of these cases, for which some theoretical and experimental contributions are provided, is the natural convection in a cylindrical enclosure heated from below, also known as the Rayleigh-Bénard problem [14, 15]. However, the information presented in these works, such as the critical Rayleigh number at which convection starts, or different flow structures depending on the non-dimensional numbers of the problem, are insufficient for a detailed verification of the code.

The main objective of this chapter is to expose the methodology employed on the development and verification of a three-dimensional cylindrical coordinates CFD code, and to present verified solutions together with their uncertainty estimates. The first involves the resolution of two cases which analytical solution is known. The latter considers the resolution of three cases: i) a $r - \theta$ coordinates test case proposed by De Vahl Davis [16] consisting in a flow induced by a tangential velocity at the boundary, ii) the natural convection in a cylindrical enclosure heated from below (Rayleigh-Bénard problem), and iii) the fluid motion between two concentric cylinders, one of them (the innermost) rotating with angular velocity ω (Couette flow with Taylor vortices). An *h-refinement* criteria and the post-processing procedure commented in previous chapter have been used to verify numerical solutions. As this procedure has still not been employed on the verification of three-dimensional cylindrical coordinates discretisation problems, its appropriateness has also been demonstrated, widening in this sense its range of applicability.

3.2   Verification of the code

In the present chapter, the *h-refinement* study carried out for each test case solved, has been usually performed to five, instead of three, consecutive meshes. Thus, the post-processing procedure commented in section 2.4 has been applied three times, once for each set of three consecutive solutions. Numerical results reported, together with their uncertainty estimates, are given for meshes which the obtained estimates are credible. As has been commented in previous chapter, estimators are credible when for a high percentage of Richardson nodes, the observed order of accuracy of the solution for each variable approaches its theoretical value. In this sense, it is important to point out, that meshes adopted for the resolution of each case have been chosen according to the results of the verification process. That is, other discretisation meshes have also been solved but solutions have been rejected due to non-credible estimators.

In order to demonstrate the applicability of this post-processing tool, two cases with analytical solutions have been analysed: a uniform parallel flow through a cylindrical geometry (Case A1) and a laminar Couette flow (Case A2). Two main aspects are hereafter discussed: i) the use of the tool in the process of code verification, pointing out its utility in the selection of the appropriate discretisation grid or numerical schemes or in detecting possible programming bugs and; ii) the use of the tool in the verification of the numerical solutions, defining their uncertainty due to discretisation. To carry out the second one, the exact global absolute discretisation error (e_D), defined as the absolute difference between the evaluated and the analytical solution weighted by the volume, has been compared with the uncertainty estimate (GCI) obtained from the post-processing procedure.

3.2.1   Case A1: Uniform flow through a cylindrical geometry.

The case consists in a uniform parallel flow through a cylindrical domain. Considering that the flow is not aligned to r or θ coordinates, this problem is specially addressed to the analysis of the singularity treatment at the axis ($r = 0$). Taking into account the geometry and flow conditions shown in Fig. 3.1, the analytical solution to this case is:

$$\vec{v} = u \, \sin\alpha \, \vec{j} + u \, \cos\alpha \, \vec{k} \tag{3.1}$$

For the resolution of the governing equations, the boundary conditions imposed
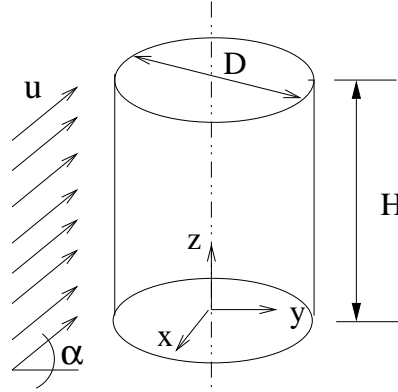
Figure 3.1: Case A1: Uniform flow. Geometry.

have been defined by the analytical solution 3.1. That is,

$$
\left.
\begin{aligned}
v_r &= u \sin \alpha \sin \theta \\
v_\theta &= u \sin \alpha \cos \theta \\
v_z &= u \cos \alpha
\end{aligned}
\right\} \quad \text{for } \theta \leq 0 \leq 2\pi; r = D/2 \tag{3.2}
$$

$$
\frac{\partial \vec{v}}{\partial \mathbf{n}} = 0 \qquad \text{for } 0 < r < D/2; z = 0 \,; z = H \tag{3.3}
$$

In the case solved, the value of the flow angle (α) has been set to: $\alpha = \pi/4$.

The non-dimensional analysis of the governing equations (see section 2.2) and the boundary conditions show that the non-dimensional group that define the case is the Reynolds number ($Re = \rho u D/\mu$), being u the fluid velocity. Thus, two different situations have been solved, considering Reynolds numbers of: $Re = 100$ and $Re = 1000$.

The computational domain has been discretised for the radial, azimuthal and axial directions using regular meshes of nxnx$(5/8n)$ control volumes. Then, the *h-refinement* study has been performed for five levels of refinement: n= 8, 16, 32, 64 and 128. That means, e.g. for the third level of refinement corresponding with $n = 32$, the mesh solved has been of 32x32x20 CVs. Aiming a comparison between numerical schemes, the first order accuracy Upwind Differencing Scheme (UDS) and the high order of accuracy SMART scheme have been used for the evaluation of the convective terms.

All the numerical results are presented in a non-dimensional form: $v_r^* = v_r/u$, $v_\theta^* = v_\theta/u$, $v_z^* = v_z/u$. Due to the flow configuration, the greater difficulty in solving

61

	Re = 100											
	v_r^*				v_θ^*				v_z^*			
grid	Rn	p	GCI	e_D	Rn	p	GCI	e_D	Rn	p	GCI	e_D
$n_3/n_2/n_1$	[%]		[%]	[%]	[%]		[%]	[%]	[%]		[%]	[%]
8/16/32	76	−0.51	55	1.73	73	0.21	20	3.25	69	1.5	0.034	0.046
16/32/64	93	0.56	5.7	0.61	92	0.4	14	1.5	75	1.2	0.026	0.029
32/64/128	95	0.8	0.19	0.08	96	0.9	0.2	0.04	84	1.07	0.016	0.018
	Re = 1000											
	v_r^*				v_θ^*				v_z^*			
grid	Rn	p	GCI	e_D	Rn	p	GCI	e_D	Rn	p	GCI	e_D
$n_3/n_2/n_1$	[%]		[%]	[%]	[%]		[%]	[%]	[%]		[%]	[%]
8/16/32	78	−0.3	28	2.1	75	0.4	11	3.5	63	1.6	0.038	0.081
16/32/64	93	0.56	6.0	0.84	89	0.4	15	1.6	64	0.85	0.069	0.059
32/64/128	96	0.88	0.28	0.09	94	0.83	0.90	0.16	86	0.95	0.033	0.035

Table 3.1: Case A1: Uniform parallel flow. Post-processing verification results. $Re = 100$ and $Re = 1000$. Numerical scheme UDS for convective terms and central differences for diffusive terms.

this case remains on the treatment of the mathematical singularity at the cylinder center. Thus, higher discrepancies are expected to occur at this location.

In Tables 3.1 and 3.2 results of the post-processing procedure for each of the numerical schemes used on the evaluation of the convective terms (UDS and SMART) are shown. The results given are for both Reynolds numbers considered. The values for the percentage of the Richardson nodes (Rn), the observed order of accuracy (p), the global GCI and the global exact discretisation error (e_D) obtained using the analytical solution, are given for each set of three consecutive meshes on the *h-refinement*. Each mesh is represented by the grid parameter n. The values for the GCI and the e_D have been normalised using the reference velocity.

As can be observed, as the level of refinement increases, the higher is the number of the Richardson nodes obtained. As convective terms are dominant in the flow nature, the observed order of accuracy must tends to the theoretical value of the numerical scheme used to evaluate those terms. That is, 1 for the UDS scheme and between 1 and 3 for the SMART scheme. Notice that in both cases (Tables 3.1 and 3.2) as the mesh is refined the order of accuracy tends to its theoretical value. The number of Richardson nodes obtained with the SMART scheme is lesser than those obtained with the UDS scheme. This is because the SMART scheme increases the number of nodes converging in an oscillatory manner.

Comparison of the exact discretisation error e_D and the GCI shows the good prediction of this estimator. As has been commented before (section 2.4), previous experience has shown that the credibility of GCI estimates depends basically on

	v_r^*				v_θ^*				v_z^*			
					Re $= 100$							
grid	Rn	p	GCI	e_D	Rn	p	GCI	e_D	Rn	p	GCI	e_D
$n_3/n_2/n_1$	[%]		[%]	[%]	[%]		[%]	[%]	[%]		[%]	[%]
8/16/32	68	1.6	9.20	0.71	55	1.8	0.65	2.77	91	1.8	0.022	0.016
16/32/64	73	1.9	0.94	0.07	70	1.1	4.10	1.33	93	1.8	0.006	0.004
32/64/128	77	1.9	0.19	0.01	87	1.6	0.65	0.04	98	1.9	0.001	0.001
					Re $= 1000$							
grid	Rn	p	GCI	e_D	Rn	p	GCI	e_D	Rn	p	GCI	e_D
$n_3/n_2/n_1$	[%]		[%]	[%]	[%]		[%]	[%]	[%]		[%]	[%]
8/16/32	65	1.7	8.00	0.73	54	1.5	1.01	2.72	86	1.8	0.025	0.017
16/32/64	71	2.0	0.78	0.07	74	1.4	2.79	1.33	92	2.0	0.006	0.004
32/64/128	76	2.0	0.16	0.01	90	1.7	0.42	0.03	98	1.9	0.001	0.001

Table 3.2: Case A1: Uniform parallel flow. Post-processing verification results. $Re = 100$ and $Re = 1000$. Numerical scheme SMART for convective terms and central differences for diffusive terms.

a good estimation of the order of accuracy of the numerical solution, and on the number of grid nodes where the application of the post-processing procedure has been possible (i.e. Richardson nodes).

An example of a wrong uncertainty estimation can also be observed in Table 3.1. When using the UDS scheme, e.g. for the third level of refinement ($n = 32$) and radial velocity v_r, even though the number of Richardson nodes is high enough ($Rn = 76\%$), the observed order of accuracy ($p = -0.51$) does not agree with the theoretical one ($p = 1$). The negative value of the observed order of accuracy could means that solution obtained it is not in the asymptotical range. In this case, *GCI* overpredicts the discretisation error ($GCI = 55\%$ vs $e_D = 1.73\%$).

Figure 3.2 shows the mean relative error weighted by the volume fraction as a function of the number of control volumes for both Reynolds numbers. As can be seen, deviations from analytical solution tends to decrease as the level of refinement increases for both numerical schemes. Notice also, that the mean relative errors obtained when using the high order of accuracy SMART scheme are lower than those obtained with the first order accuracy scheme for the same grid.
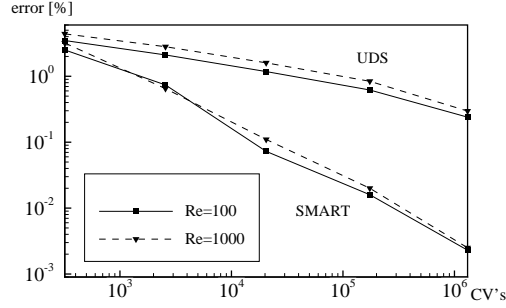
Figure 3.2: Case A1: Uniform flow. Mean relative error of the velocity vector weighted by the volume fraction as a function of the number of control volumes. Solid line, $Re = 100$; dashed line, $Re = 1000$.

3.2.2   Case A2: Laminar Couette flow.

The fluid motion in the gap between two infinite concentric cylinders, one or both are rotating along their common axis, is known as the Couette flow. There are several flow regimes existing in an incompressible fluid between two concentric rotating cylinders. Hydrodynamic instabilities and flow transition between regimes are determined for the Reynolds number of the two cylinders, the geometry, and the initial conditions [11, 12]. The flow regimes consist of different spatial and temporal patterns. According to [17] most flows are non-stationary and non-axisymmetric, except for the simplest flow regimes of the circular Couette flow and the Couette-flow with Taylor vortices.

An schematic of the problem geometry is shown in Fig. 3.3. For low-Reynolds numbers, an analytical solution can be obtained. Being ω_i and ω_o the inner and outer cylinder angular velocities, the analytical steady state solution for this Couette problem is:

$$v_\theta(r) = r_i\omega_i \frac{r_0/r - r/r_0}{r_0/r_i - r_i/r_0} + r_0\omega_0 \frac{r/r_i - r_i/r}{r_0/r_i - r_i/r_0} \tag{3.4}$$

This solution corresponds to a set of vortices forming concentric annulus for azimuthal velocity. The radial and axial velocities (v_r and v_z), become zero for the whole domain.

The dimensionless numbers that define the problem are: the Reynolds numbers (referred to the inner and outer cylinder), $Re_i = \rho r_i \omega_i (r_o - r_i)/\mu$ and $Re_o = \rho r_o \omega_o (r_o - r_i)/\mu$; and the radius ratio ($r_i/r_o$). The case solved here has been reported

64
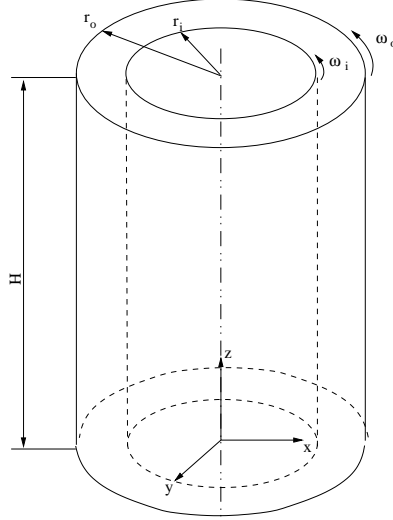
Figure 3.3: Case A2: Laminar Couette flow. Geometry

by [18] and corresponds with a $Re_i = 350$ and $Re_o = -690$ (negative Reynolds number represents a cylinder with clockwise rotation), and a radius ratio of $r_i/r_o = 0.883$.

Boundary conditions imposed have been azimuthal velocities at the boundaries ($r = r_i$ and $r = r_o$) defined by Eq. 3.4, while derivatives of the dependent variables at the z-direction ($z = 0$ and $z = H$) have been taken null ($\partial\phi/\partial z = 0$).

$$\left.\begin{aligned} v_r &= 0 \\ v_\theta &= r_i\,\omega_i \\ v_z &= 0 \end{aligned}\right\} \qquad \text{for } r = r_i;\, \forall\,\{\theta, z\} \tag{3.5}$$

$$\left.\begin{aligned} v_r &= 0 \\ v_\theta &= r_o\,\omega_o \\ v_z &= 0 \end{aligned}\right\} \qquad \text{for } r = r_0;\, \forall\,\{\theta, z\} \tag{3.6}$$

$$\frac{\partial\phi}{\partial\mathbf{n}} = 0 \qquad \text{for } z = 0\,;\, z = H;\, \forall\{r_i < r < r_0, \theta\} \tag{3.7}$$

Due to the one-dimensional flow structure (radial and axial velocity components are zero for the steady state solution), the number of control volumes at z- direction and at θ-direction have been fixed to 20. Hence, the *h-refinement* study has been performed for regular meshes of n control volumes in radial direction with $n = 6$, 12, 24, 48 and 96.

65
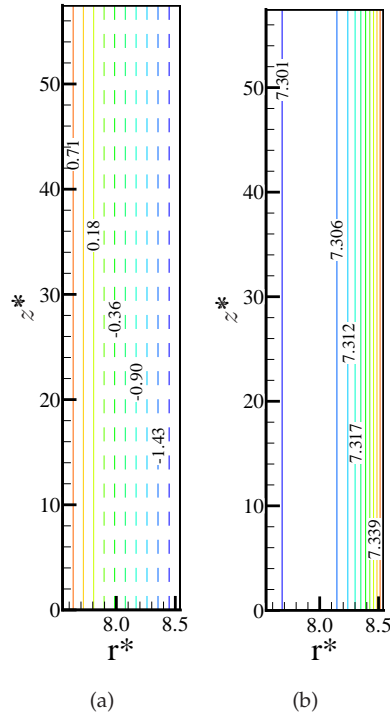
Figure 3.4: Case A2: Laminar Couette flow. Steady state solution contours for non-dimensional (a) azimuthal velocity v_θ, (b) dynamic pressure p_d (right) at an arbitrary azimuthal plane. $Re_i = 350$, $Re_o = -690$.

The structure of the steady circular flow pattern is shown in Fig. 3.4. In the figure, as axial and radial velocity components are zero, are only plotted the non-dimensional azimuthal velocity component ($v_{\theta*} = v_\theta/v_{\theta,i}$) and pressure.

In Table 3.3, results of the post-processing verification procedure are given. As can be seen, estimation of the order of accuracy is around 2 with a 100% of Richardson nodes. The imposed boundary conditions imply that only diffusive forces are present. Thus, the observed order of accuracy must tends to the theoretical one for a central difference scheme ($p = 2$). The exact discretisation error, e_D, obtained from the analytical solution is well estimated by the GCI. The agreement observed between both numerical and analytical solutions is adequate even for the coarsest grid.

grid	$v_\theta^* = v_\theta / v_{\theta i}$			
	Rn	p	GCI	e_D
$n_3/n_2/n_1$	[%]		[%]	[%]
6/12/24	100	2.0	$2.8\text{x}10^{-2}$	$2.4\text{x}10^{-2}$
12/24/48	100	2.0	$7.4\text{x}10^{-3}$	$5.9\text{x}10^{-3}$
24/48/96	100	2.0	$1.8\text{x}10^{-3}$	$1.5\text{x}10^{-3}$

Table 3.3: Case A2: Laminar Couette flow. Post-processing verification results. Numerical scheme SMART for convective terms and central differences for diffusive terms.

In addition, another steady circular Couette flow case has been solved, varying the Reynolds number and the radius ratio. This situation corresponds to Reynolds numbers for the inner and outer cylinders of: $Re_i = 20$ and $Re_o = 0$ and a radius ratio $r_i/r_o = 0.667$. Results obtained for this situation have been similar to the aforementioned case. This means that, for all the levels of refinement the order of accuracy has been 2 with approximately a 100% of Richardson nodes, being the GCI for the finest mesh of $1.3\text{x}10^{-3}$ %.

3.2.3 Further remarks

Results of the cases with analytical solution presented have shown that the estimators predicted by the post-processing procedure agree well with the exact computational error (e_D), being adequate its application on cylindrical coordinates cases. On the other hand, the errors introduced with the treatment of the boundary conditions imposed at the cylinder center (case A1) decreases with the refinement of the mesh.

Furthermore, the application of this post-processing procedure has been helpful during the development of the code to find out pre-existing code bugs or mistakes, that forces the obtention of solutions with observed order of accuracy different than the expected theoretical value (e.g. inappropiate arrays indexation) or even for selecting an appropriate boundary condition treatment. For example, during the development of the code, in the formulation of the spatially periodic boundary condition in the azimuthal direction, two control volumes were considered for the overlapping zone (see section 2.3.3). However, the observed order of accuracy of the numerical results when the high order numerical scheme SMART was used tended to 1. Discrepancies with the expected value of the order of accuracy were found in a wrong treatment of this condition. In this case, differences were due to the manner that convective terms were evaluated in the overlapping zone (forcing a first order of accuracy scheme). As a result, to assure an accurate solution, four control

volumes, instead of two, have been added in the overlapping zone. The approach implemented has allowed to calculate the whole domain with the same order of accuracy.

Considering the results obtained with the cases with analytical solution studied, this post-processing procedure is applied, hereafter, in the verification of the numerical solutions of different cases in cylindrical coordinates.

3.3 Verified numerical results of different test cases

Three problems have been selected: a $r - \theta$ induced flow by a tangential velocity at the boundary (Case B1); the natural convection in a cylindrical enclosure heated from below (Rayleigh-Bénard problem) (Case B2); and the fluid motion between two concentric rotating cylinders (laminar Couette flow with Taylor vortices) (Case B3). For each particular case, the value of the governing parameters, dimensionless numbers, specific boundary conditions, and the discretisation employed are presented. All cases have been solved using an *h-refinement* criteria, and uncertainty estimators have been obtained from the post-processing procedure. In all cases, verified numerical solutions for the highest level of refinement are provided.

3.3.1 Case B1: Induced flow by a tangential velocity at the boundary.

The fluid motion induced by the movement of the outer boundary of the cylinder in the circumferential direction proposed by De Vahl-Davis [16] has been analysed. One half of the domain is moving clockwise and the other half counterclockwise (see Fig. 3.5a). Being ω the tangential velocity of the boundary of a cylinder of height H, boundary conditions can be written as follows:

$$
\begin{aligned}
v_r &= 0 & &\text{at } r = R \,; \forall\{\theta, z\} \\
v_\theta &= -w & &\text{at } r = R \,; \forall\{-\pi/2 < \theta < \pi/2, z\} \\
v_\theta &= w & &\text{at } r = R \,; \forall\{\pi/2 < \theta < 3\pi/2, z\} \\
v_\theta &= 0 & &\text{at } r = R \,; \theta = \pi/2 \text{ or } 3\pi/2 \,, \forall\{z\} \\
\frac{\partial \vec{v}}{\partial z} &= 0 & &\text{at } z = 0 \,, z = H \,, \forall\{\theta, r\}
\end{aligned}
\tag{3.8}
$$

With the objective to compare the numerical solution with the one reported by De Vahl Davis, two Reynolds numbers ($Re = \rho\omega R/\mu$) have been analysed: $Re = 1$ and $Re = 10$.

Figure 3.5: Case B1: Induced flow by a tangential velocity at the boundary. (a) Geometry. (b) Half computational domain and mesh details (number of grid nodes and concentration).

The steady state solution of this problem is two-dimensional (r-θ directions), being axial velocity component (v_z) zero. Taking into account this particularity, in the discretisation of the domain at z-direction, the number of control volumes has been fixed to 20 and the length of the domain in this direction has been arbitrary (H). For r-θ directions, the mesh has been concentrated around the vertical diameter ($x = 0, y$, see Fig. 3.5b), and at the external radius where azimuthal velocity gradients are the largest. To do this, the domain has been divided into different zones (marked with Roman numbers in Fig. 3.5b) introducing a higher number of nodes where has been considered necessary. Moreover, in these zones the mesh has been concentrated by means of a tanh-like function with a concentration factor of 1 or 2 depending on the zone. In r-direction, the concentration factor for zones IV, V and VI has been set to 1, while for the zones close to the wall (I, II and III) it has been set to 2. In θ-direction, for zones I, III, IV and VI, a concentration factor of 1 has been adopted. All these zones where the mesh has been concentrated are marked with black triangles in Fig. 3.5b.

Once the domain is discretised, the *h-refinement* study has been performed for meshes of nx($8/5n$)x20 control volumes with five levels of refinement ($n = 10$, 20,

(a)

(b)
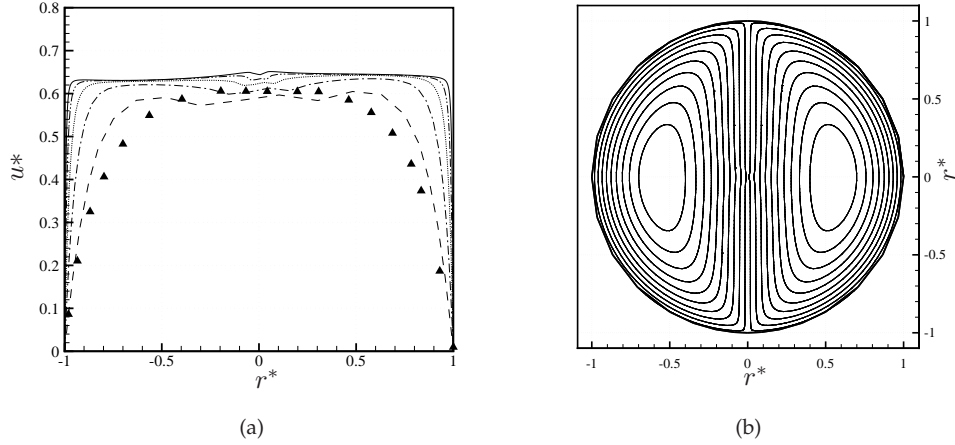
Figure 3.6: Case B1: Induced flow by a tangential velocity at the boundary. $Re = 1$. (a) Radial velocity along the vertical diameter $(x = 0, y)$ for different grids (n). $(--)$ Dashed line, $n = 10$; $(-\cdot-)$ dash-dot line, $n = 20$; $(\cdots)$ dotted line, $n = 40$; $(-\cdot\cdot-)$ dash-dot-dot line, $n = 80$; $(-)$ solid line, $n = 160$; (▲) De Vahl Davis solution (15x24) [16]. (b) Streamlines for $n = 80$ (80x128x20 grid)

40, 80, 160). This means that for $n = 80$, the domain has been solved for a grid of 80x128x20 control volumes in the r-θ plane. Numerical results are presented in a non-dimensional form: $v_r^* = v_r/\omega$, $v_\theta^* = v_\theta/\omega$.

Velocities along the vertical diameter $(x = 0, y)$ for all grids and $Re = 1$ are plotted in Fig. 3.6a. As can be seen, the deviation around the axis tends to decrease as the grid is refined, and differences between meshes 4 and 5 become visually negligible. De Vahl Davis solution is also shown. Numerical results do not adjust well with De Vahl Davis solution, but as has been mentioned in his work, these results did not correspond with a grid independent solution (the grid used in his work has been of 15x24 control volumes). This solution has been only taken as an illustrative result to point out the necessity of computation verification. In Fig. 3.6b, streamlines distribution obtained for the level of refinement $n = 80$ is shown as an illustrative result of the flow pattern.

Results of the verification process for both Reynolds number are shown in Table 3.4. As for the steady state solution of the case (axial velocity v_z becomes zero), results arising from the post-processing procedure are given only for radial and azimuthal velocity components. For the level of refinement $n = 160$, in both cases, a

70

grid $n_3/n_2/n_1$	v_r^*				v_θ^*		
$Re = 1$							
	Rn [%]	p	GCI [%]		Rn [%]	p	GCI [%]
10/20/40	78	1.4	1.10		85	1.3	1.90
20/40/80	87	1.5	0.34		89	1.7	0.25
40/80/160	94	1.7	0.07		91	1.7	0.05
$Re = 10$							
	Rn [%]	p	GCI [%]		Rn [%]	p	GCI [%]
10/20/40	79	1.2	2.10		88	1.3	3.00
20/40/80	88	1.5	0.36		94	1.9	0.33
40/80/160	94	1.7	0.09		90	1.8	0.10

Table 3.4: Case B1: Induced flow by a tangential velocity at the boundary. Post-processing verification results. Numerical scheme SMART for convective terms and central differences for diffusive terms. (For table description see section 2.4).

high percentage of Richardson nodes has been achieved. The observed order of accuracy of the solution agree well with the theoretical one considering the numerical scheme used for the convective terms (SMART). Global *GCIs* estimate an uncertainty due to discretisation lower than 0.1% for all variables and both Reynolds numbers.

The results of the non-dimensional radial velocity and non-dimensional azimuthal velocity are given in Table 3.5. The values for the non-dimensional radial velocity component have been obtained along vertical plane ($x = 0, y$) and for the non-dimensional azimuthal velocity component along horizontal plane ($x, y = 0$). All the results shown are given for the highest level of refinement (i.e. for $n = 160$) and both Reynolds numbers considered. Notice that velocities are given together with their uncertainty estimates (error band), corresponding to the *GCI* values calculated for the mesh for which the results are given ($n = 160$, see Table 3.4).

.	Re $= 1$		Re $= 10$	
r	$v_r^* \pm 0.07\%$	$v_\theta^* \pm 0.05\%$	$v_r^* \pm 0.09\%$	$v_\theta^* \pm 0.10\%$
-0.95	-0.300	0.887	-0.298	0.888
-0.85	-0.617	0.662	-0.633	0.663
-0.75	-0.636	0.439	-0.683	0.441
-0.65	-0.641	0.222	-0.699	0.225
-0.55	-0.644	0.015	-0.704	0.019
-0.45	-0.645	-0.177	-0.703	-0.172
-0.35	-0.646	-0.346	-0.698	-0.343
-0.25	-0.647	-0.484	-0.690	-0.485
-0.15	-0.649	-0.584	-0.681	-0.591
-0.05	-0.650	-0.645	-0.674	-0.655
0.05	0.648	0.645	0.657	0.655
0.15	0.645	0.584	0.638	0.592
0.25	0.640	0.484	0.619	0.487
0.35	0.636	0.346	0.602	0.344
0.45	0.634	0.177	0.589	0.172
0.55	0.632	-0.015	0.579	-0.020
0.65	0.630	-0.222	0.575	-0.227
0.75	0.630	-0.439	0.576	-0.443
0.85	0.627	-0.662	0.581	-0.664
0.95	0.312	-0.887	0.292	-0.888

Table 3.5: Case B1: Induced flow by a tangential velocity at the boundary. Velocity components for $Re = 1$ and $Re = 10$. Non-dimensional radial velocity component at vertical plane $(x = 0, y)$ and non-dimensional azimuthal velocity component at horizontal plane $(x, y = 0)$. Level of refinement $n = 160$.

3.3.2 Case B2: Rayleigh-Bénard problem.

The fluid flow inside a vertical cylinder of aspect ratio $A = H/D$, heated from below is also known as Rayleigh-Bénard convection. Because of natural convection inside enclosures plays an important role in many technical applications (solar energy, crystal growth, micro-electronics), this phenomenon has been widely treated in literature [19, 14, 15, 20]. The boundary conditions that close the problem can be summarised as follows:

$$\left. \begin{array}{l} \vec{v} = 0 \\ T = T_h \end{array} \right\} \qquad \text{for } z = 0; \forall \{r, \theta\} \tag{3.9}$$

$$\left. \begin{array}{l} \vec{v} = 0 \\ T = T_c \end{array} \right\} \qquad \text{for } z = H; \forall \{r, \theta\} \tag{3.10}$$

$$\left. \begin{array}{l} \vec{v} = 0 \\ \dfrac{\partial T}{\partial \mathbf{n}} = 0 \end{array} \right\} \qquad \text{for } r = D/2; \forall \{\theta, z\} \tag{3.11}$$

where T_c and T_h are the imposed temperatures at top and bottom walls respectively (being $T_h > T_c$).

From the non-dimensionalisation of the governing equations and boundary conditions arise that the natural convection of the fluid inside the cavity is characterised by three dimesionless numbers:

$$\text{Rayleigh number,} \quad Ra = \frac{\rho g \beta (T_h - T_c) H^3}{\alpha \mu}$$

$$\text{Prandtl number,} \quad Pr = \frac{\mu}{\rho \alpha} \tag{3.12}$$

$$\text{aspect ratio,} \quad A = \frac{H}{D}$$

The onset of convection takes place when the Rayleigh number reach certain critical value ($Ra > Ra_{cr}$). For low Rayleigh numbers ($Ra < Ra_{cr}$), the fluid is stratified and heat transfer is driven only by conduction. For aspects ratios lower than 1, convection sets with axisymmetric flow configuration and as the Rayleigh number increases, a transition from axisymmetric to three-dimensional non-axisymmetric convection occurs ($Ra > Ra_{cr,3D}$). If the Rayleigh number exceeds this critical value, the axisymmetric solution is unstable and bifurcates to the stable non-axisymmetric one [14, 15]. For aspects ratios greater than 1, convection is always non-axisymmetric.

In the present thesis, the problem has been solved for an aspect ratio $A = 0.5$, a Prandtl number of $Pr = 6.7$ and for different Rayleigh numbers in the range within:
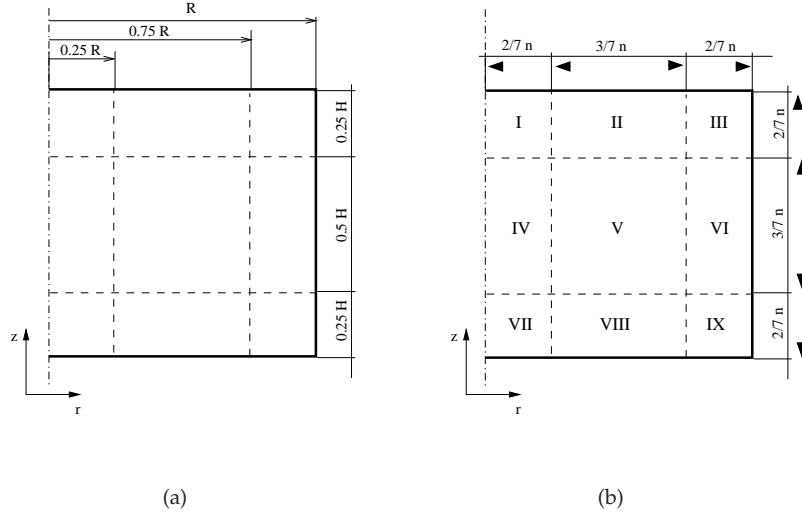
Figure 3.7: Case B2: Rayleigh-Bénard problem. (a) Geometry. (b) Mesh and computational domain

$Ra = 2200 \div 15000$. No fluid motion at $t = 0$ and initial temperature $T_0 = T_c$ have been imposed. Adiabatic lateral walls and non-slip conditions for all walls have been assumed.

Considering the flow structure, non-uniformly distributed meshes of nx$(6/7n)$xn control volumes have been used to solve the case. In this sense, the computational domain has been divided into different zones, increasing the grid nodes distribution near the walls and on the axis (see Fig. 3.7). Moreover, it has been also considered necessary to concentrate the grid at the central zones, this means, at z-direction (zones IV, V and VI) and at r-direction (zones II, V and $VIII$). Those zones are marked with a black triangle and the concentration factor has been set to 1. In the azimuthal direction a regular distribution of nodes has been adopted. Details of the number of grid nodes and concentration areas are given in Fig. 3.7.

As has been commented before, depending on the boundary conditions different flow regimes can be obtained: i) axisymmetric and ii) non-axisymmetric flow configuration. For axisymmetric flow configuration, and depending also on initial conditions, two equivalent solutions can be found [15], one with upflow and one with downflow at the center of the cavity. According to the initial conditions imposed in this work, the axisymmetric flow pattern obtained consist of one-toroidal

Figure 3.8: Case B2: Rayleigh-Bénard convection. Axialsymmetric flow configuration. $Ra = 2800$. (a) Axial velocity (v_z) and (b) temperature contours.

roll with downflow at the center of the cylinder. As an illustrative example of the axisymmetric flow configuration, the axial velocity (v_z) and temperatures contours for this situation are shown in Fig. 3.8.

The non-axisymmetric flow consists of two symmetric rolls ascending along the cylinder walls with downstream at their symmetry plane. Details of the flow structure for this situation are shown in Fig. 3.9, where the axial velocity (v_z) and temperature contours are plotted.

For the set of cases solved, the onset of convection has been detected to occur at $Ra = 2245$. This result is in good agreement ($\approx 0.6\%$) with the values obtained from linear stability theory for the non-slip boundary conditions, that predicts a critical value for the Rayleigh number of $Ra_{cr} = 2260$, for an aspect ratio $A = 0.5$ [21]. The transition from the axisymmetric to non-axisymmetric flow structure has been detected beyond $Ra = 8000$. However, detailed studies for determining this transition point have not been carried out in the present work.

Numerical solutions of all cases considered corresponding with the different Rayleigh numbers selected (in the range $Ra = 2200 \div 15000$), have been submitted to the process of verification using five levels of refinement ($n = 7, 14, 28, 56$ and 112). In all cases, convective terms have been evaluated by means of the SMART scheme, while for diffusive terms a central difference scheme has been used.

Hereafter, the results for the axisymmetric and non-axisymmetric flow configurations are given. All the results presented are in non-dimensional form, according

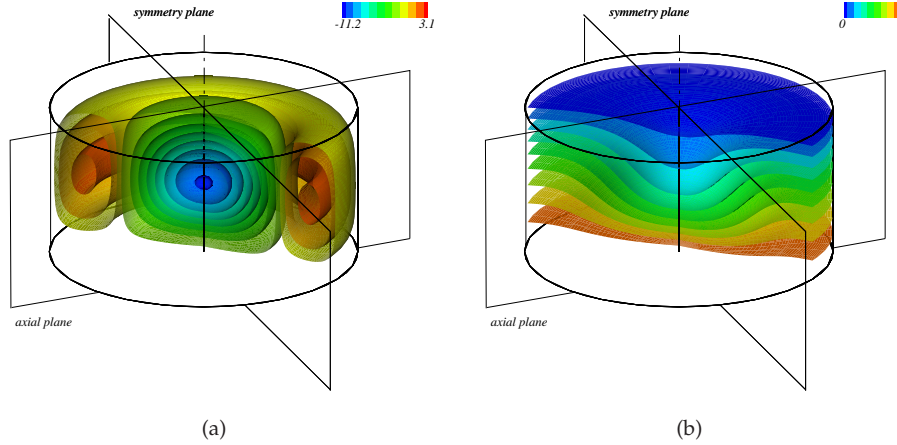(a)   (b)
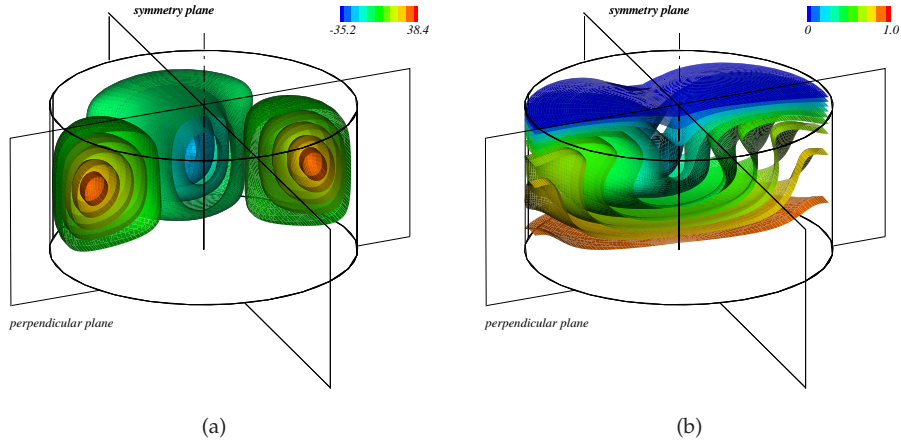
Figure 3.9: Case B2: Rayleigh-Bénard convection. Non-axisymmetric flow config-
uration. $Ra = 15000$. (a) Axial velocity (v_z) and (b) temperature contours.

the non-dimensionalisation of the governing equations considered. That is, non-
dimensional coordinates, velocities and temperatures are defined according to: $r^* = r/H$; $z^* = z/H$; $\vec{v}^* = \vec{v}/(\alpha/H)$; $\Theta = (T - T_c)/(T_h - T_c)$.

Axialsymmetric flow pattern results

As has been commented before, axisymmetric flow configurations have been ob-
tained for a range of Rayleigh numbers between $Ra = 2800 \div 8000$. As an illustrative
example of the solutions obtained, the dimensionless components of the velocities
and temperatures are plotted for the different levels of refinement for $Ra = 2800$ in
Fig. 3.10. The results shown in the figure correspond with two different planes, at
$r^* = 0.5$ and $z^* = 0.5$, according with Fig. 3.11.

As can be observed, even for the coarsest meshes, high concordance between the
solutions for the different meshes is obtained. Differences between levels of refine-
ment, corresponding with grid parameter $n = 56$ and $n = 112$, are visually negligible
for all variables.
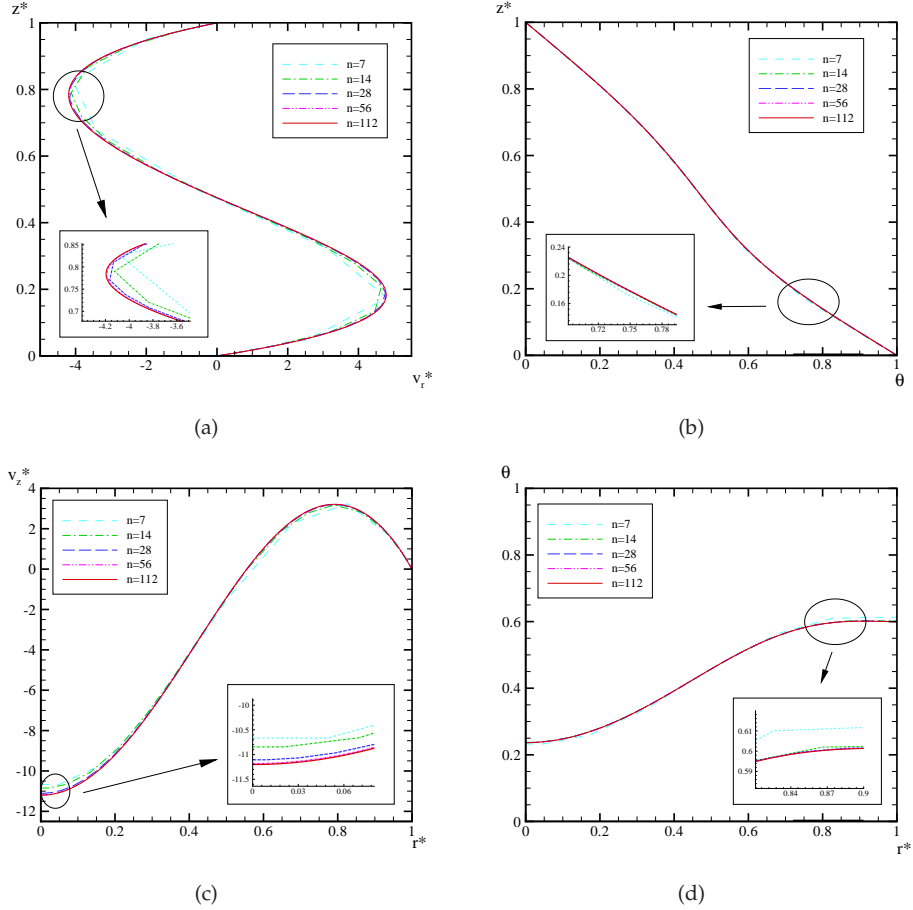
Figure 3.10: Case B2: Rayleigh-Bénard convection. $Ra = 2800$. Results of the *h-refinement* study (a) Non-dimensional radial velocity component at $r^* = 0.5$. (b) Non-dimensional temperature at $r^* = 0.5$. (c) Non-dimensional axial velocity component at $z^* = 0.5$. (d) Non-dimensional temperature at $z^* = 0.5$

Results of the verification process for cases in this range, for radial and axial velocity components (v_r^* and v_z^*) and for temperature variable are given in Table 3.6. Since the steady state solution in this range is axisymmetric, azimuthal velocity component obtained has been zero ($v_\theta = 0$). Thus, verification results for this velocity component are meaningful. Highly satisfactory results have been obtained for all
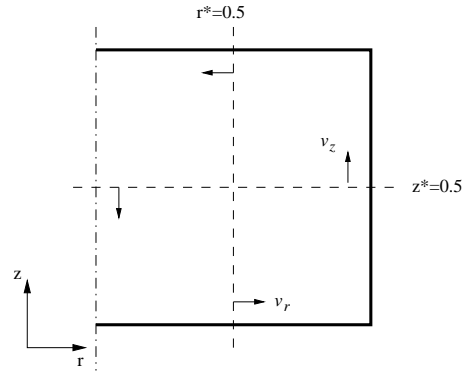
Figure 3.11: Case B2: Rayleigh-Béenard convection. Schematic of representation of velocity components in an arbitrary axial plane

cases in the range studied. In all cases a great number of Richardson nodes has been obtained, even for medium grid ($n = 28$). The order of accuracy of the solution in all cases tends to its theoretical value (between 1 and 3 for SMART scheme), as the mesh is refined.

In Table 3.7, the results of the non-zero non-dimensional velocity components (v_r^* and v_z^*) and temperature (Θ) are given. Velocities and temperature are given at the vertical ($r^* = 0.5, z^*$) and horizontal middle lines ($r^*, z^* = 0.5$) of an arbitrary axial plane (r, z) (see Fig. 3.11).

All the numerical results presented, together with their uncertainty estimates, have been obtained for the the highest level of refinement ($n = 112$). To a better understanding of the flow pattern obtained in this range (one roll with downflow at the cylinder axis), in Fig. 3.12 are represented velocity vector and temperature profiles for $Ra = 2800$, for an arbitrary axial plane.

				$Ra = 2800$						
		v_r^*			v_z^*			Θ		
grid	Rn	p	GCI	Rn	p	GCI	Rn	p	GCI
$n_3/n_2/n_1$	[%]		[%]	[%]		[%]	[%]		[%]
7/14/28	90	2.0	1.30	94	1.5	3.00	96	1.7	0.088
14/28/56	92	1.9	0.36	94	1.8	0.48	97	1.9	0.015
28/56/112	93	2.2	0.06	94	2.2	0.06	96	2.7	0.001
				$Ra = 4000$						
		v_r^*			v_z^*			Θ		
grid	Rn	p	GCI	Rn	p	GCI	Rn	p	GCI
$n_3/n_2/n_1$	[%]		[%]	[%]		[%]	[%]		[%]
7/14/28	80	1.7	3.50	94	1.2	7.60	80	1.7	0.100
14/28/56	91	1.8	0.71	93	1.8	0.86	87	2.0	0.020
28/56/112	96	1.9	0.14	96	1.9	0.17	87	1.9	0.006
				$Ra = 6000$						
		v_r^*			v_z^*			Θ		
grid	Rn	p	GCI	Rn	p	GCI	Rn	p	GCI
$n_3/n_2/n_1$	[%]		[%]	[%]		[%]	[%]		[%]
7/14/28	78	1.7	5.30	88	1.4	8.50	80	1.7	0.110
14/28/56	91	1.8	1.10	93	1.8	1.20	88	1.7	0.032
28/56/112	96	1.9	0.22	96	1.9	0.24	92	1.8	0.007
				$Ra = 8000$						
		v_r^*			v_z^*			Θ		
grid	Rn	p	GCI	Rn	p	GCI	Rn	p	GCI
$n_3/n_2/n_1$	[%]		[%]	[%]		[%]	[%]		[%]
7/14/28	84	1.5	7.70	86	1.4	10.0	76	1.8	0.120
14/28/56	92	1.8	1.39	91	1.7	1.60	90	1.7	0.034
28/56/112	96	1.9	0.28	95	1.9	0.30	93	1.9	0.007

Table 3.6: Case B2: Rayleigh-Bénard problem. ($Ra = 2800 \div 8000$). Post-processing verification results. Numerical scheme SMART for convective terms and central differences for diffusive terms.

Table 3.7: Case B2: Rayleigh-Bénard convection. Numerical solution and uncertainty estimates for Rayleigh numbers $Ra = 2800, 4000, 6000, 8000$. Nondimensional radial velocity (v_r^*) and temperature (Θ) at $r^* = 0.5$ and nondimensional axial velocity (v_z^*) and temperature (Θ) at $z^* = 0.5$. (For details see Fig. 3.11). Level of refinement $n = 112$

$Ra = 2800$					
z^*	$v_r^* \pm 0.06\%$	$\Theta \pm 0.001\%$	r^*	$v_z^* \pm 0.06\%$	$\Theta \pm 0.001\%$
0.00	0.000	1.0000	0.00	-11.214	0.2643
0.05	2.473	0.9203	0.05	-11.085	0.2672
0.15	4.669	0.7656	0.15	-10.071	0.2898
0.25	4.386	0.6335	0.25	-8.168	0.3328
0.35	2.734	0.5340	0.35	-5.628	0.3914
0.45	0.554	0.4587	0.45	-2.803	0.4587
0.55	-1.566	0.3916	0.55	-0.120	0.5262
0.65	-3.230	0.3203	0.65	1.977	0.5841
0.75	-4.128	0.2390	0.75	3.101	0.6243
0.85	-3.897	0.1477	0.85	2.982	0.6435
0.95	-1.937	0.0499	0.95	1.416	0.6462
1.00	0.000	0.0000	1.00	0.000	0.6455
$Ra = 4000$					
z^*	$v_r^* \pm 0.14\%$	$\Theta \pm 0.006\%$	r^*	$v_z^* \pm 0.17\%$	$\Theta \pm 0.006\%$
0.00	0.000	1.0000	0.00	-21.324	0.2070
0.05	5.151	0.8839	0.05	-21.087	0.2107
0.15	9.521	0.6699	0.15	-19.225	0.2395
0.25	8.623	0.5287	0.25	-15.748	0.2922
0.35	5.073	0.4667	0.35	-11.098	0.3618
0.45	0.730	0.4418	0.45	-5.844	0.4418
0.55	-3.293	0.4150	0.55	-0.671	0.5259
0.65	-6.370	0.3661	0.65	3.614	0.6058
0.75	-8.005	0.2880	0.75	6.134	0.6691
0.85	-7.529	0.1835	0.85	6.113	0.7042
0.95	-3.751	0.0626	0.95	2.953	0.7116
1.00	0.000	0.0000	1.00	0.000	0.7108

Table 3.7: Case B2: Rayleigh-Bénard convection. Numerical solution and uncertainty estimates for Rayleigh numbers $Ra = 2800, 4000, 6000, 8000$. Non-dimensional radial velocity (v_r^*) and temperature (Θ) at $r^* = 0.5$ and non-dimensional axial velocity (v_z^*) and temperature (Θ) at $z^* = 0.5$. (For details see Fig. 3.11). Level of refinement $n = 112$

z^*	$v_r^* \pm 0.22\%$	$\Theta \pm 0.007\%$	r^*	$v_z^* \pm 0.24\%$	$\Theta \pm 0.007\%$
		$Ra = 6000$			
0.00	0.000	1.0000	0.00	−34.600	0.2045
0.05	8.317	0.8522	0.05	−34.158	0.2099
0.15	15.173	0.5957	0.15	−30.755	0.2500
0.25	13.436	0.4710	0.25	−24.686	0.3172
0.35	7.676	0.4550	0.35	−17.072	0.3940
0.45	0.926	0.4695	0.45	−8.964	0.4695
0.55	−5.203	0.4696	0.55	−1.203	0.5428
0.65	−9.891	0.4349	0.65	5.355	0.6171
0.75	−12.448	0.3551	0.75	9.506	0.6864
0.85	−11.798	0.2314	0.85	9.769	0.7329
0.95	−5.932	0.0796	0.95	4.806	0.7465
1.00	0.000	0.0000	1.00	0.000	0.7462

z^*	$v_r^* \pm 0.28\%$	$\Theta \pm 0.007\%$	r^*	$v_z^* \pm 0.3\%$	$\Theta \pm 0.007\%$
		$Ra = 8000$			
0.00	0.000	1.0000	0.00	−46.752	0.2080
0.05	10.849	0.8352	0.05	−46.060	0.2151
0.15	19.615	0.5626	0.15	−40.811	0.2673
0.25	17.094	0.4601	0.25	−31.841	0.3488
0.35	9.555	0.4709	0.35	−21.287	0.4319
0.45	0.969	0.5014	0.45	−10.826	0.5014
0.55	−6.706	0.5118	0.55	−1.325	0.5605
0.65	−12.555	0.4835	0.65	6.650	0.6219
0.75	−15.799	0.4026	0.75	11.936	0.6880
0.85	−15.054	0.2662	0.85	12.507	0.7395
0.95	−7.621	0.0920	0.95	6.236	0.7574
1.00	0.000	0.0000	1.00	0.000	0.7575

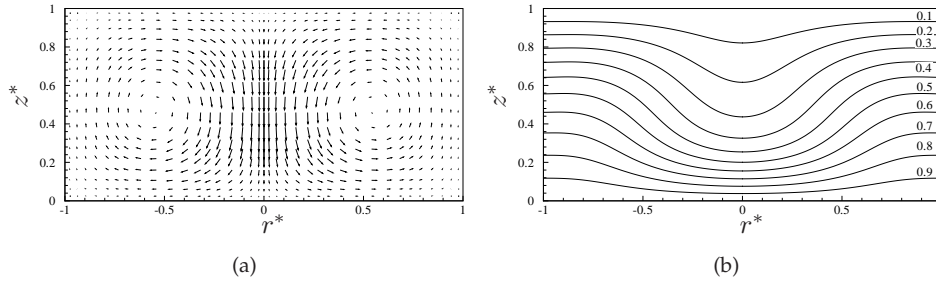(a)   (b)

Figure 3.12: Case B2: Rayleigh-Bénard convection. $Ra = 2800$. Axisymmetric flow structure. (a) Velocity field. (b) Temperature profile.

Non-axisymmetric flow pattern results

The results of the verification process for the non-axisymmetric configuration are given in Table 3.8. The verification process corresponds with $Ra = 15000$. In this case, since all velocity components have non-zero values, the verification process has been carried out for the three components of the velocity vector and the temperature. For the coarsest meshes, high discretisation errors are obtained. However, as the mesh is refined these errors tends to decrease. For the finest level of refinement, the observed order of accuracy has acceptable values with a high percentage of Richardson nodes which makes reliable the discretisation errors obtained with the finest mesh.

The non-axisymmetric velocity vector and temperature field at different planes for $Ra = 15000$ are represented in Fig. 3.13. In order to construct the flow patterns plotted, first the flow symmetry plane has been located. Thus, velocity vector and temperature profiles are given for this plane and its perpendicular one.

The verified solutions obtained with the highest level of refinement (the finest mesh, $n = 112$), for each velocity component and temperature together with their uncertainty estimates, are given in Table 3.9 . In the table, radial velocity component is evaluated at $(r^* = 0.5, z^*)$ lines of both planes, while azimuthal and axial velocity components at $(r^*, z^* = 0.5)$.

82

grid	v_r^*			v_z^*			v_θ^*			Θ		
$n_3/n_2/n_1$	Rn [%]	p	GCI [%]	Rn [%]	p	GCI [%]	Rn [%]	p	GCI [%]	Rn [%]	p	GCI [%]
7/14/28	78	1.5	40.0	70	1.4	51.0	40	1.5	24.0	69	0.9	10.0
14/28/56	69	1.5	35.0	78	1.4	14.0	88	1.3	20.0	77	1.4	1.50
28/56/112	77	1.7	6.10	75	1.6	5.30	70	1.8	2.90	72	1.5	0.53

Table 3.8: Case B2: Rayleigh-Bénard convection. $Ra = 15000$. Post-processing verification results. Numerical scheme SMART for convective terms and central differences for diffusive terms.
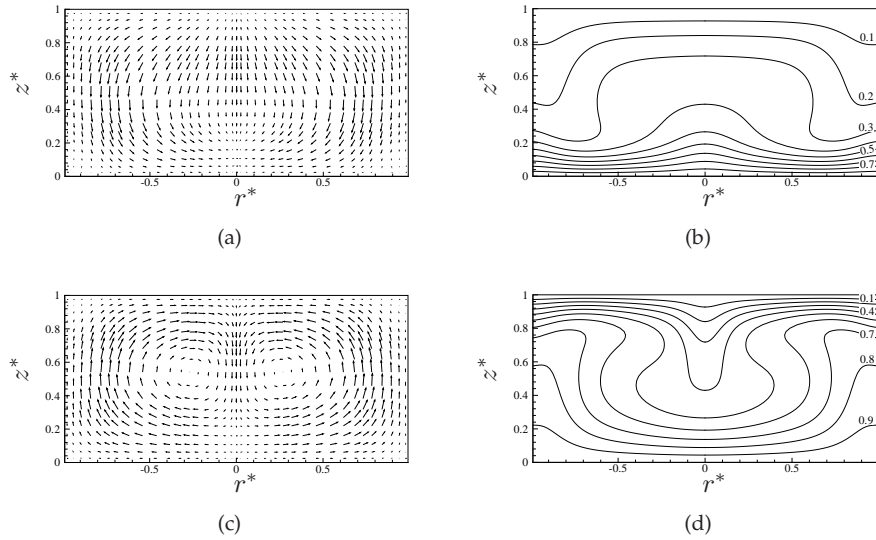

(a)

(b)

(c)

(d)

Figure 3.13: Case B2: Rayleigh-Bénard convection. $Ra = 15000$. Non-axisymmetric flow structure at different planes. (a) Velocity field and (b) temperature profile at the symmetry plane. (c) Velocity field and (d) temperature profile at the plane perpendicular to the symmetry plane.

	radial velocity component v_r^*			
	symmetry plane		perpendicular plane	
z^*	$v_r^* \pm 6.1\%$	$\Theta \pm 0.53\%$	$v_r^* \pm 6.1\%$	$\Theta \pm 0.53\%$
0.00	0.00	1.000	0.00	1.000
0.05	-7.95	0.790	10.89	0.911
0.15	-14.67	0.459	21.82	0.750
0.25	-13.17	0.354	22.56	0.625
0.35	-7.59	0.352	17.01	0.549
0.45	-0.77	0.352	7.73	0.520
0.55	5.68	0.338	-3.43	0.529
0.65	10.89	0.310	-14.56	0.564
0.75	13.97	0.253	-22.91	0.597
0.85	13.38	0.172	-24.33	0.518
0.95	6.62	0.063	-12.85	0.204
1.00	0.00	0.000	0.00	0.000
	axial velocity component v_z^*			
	symmetry plane		perpendicular plane	
r^*	$v_z^* \pm 5.3\%$	$\Theta \pm 0.53\%$	$v_z^* \pm 5.3\%$	$\Theta \pm 0.53\%$
0.00	-15.28	0.394	-15.28	0.394
0.05	-15.77	0.393	-14.73	0.398
0.15	-16.97	0.388	-8.84	0.423
0.25	-19.00	0.380	-0.67	0.454
0.35	-21.56	0.369	7.34	0.484
0.45	-24.78	0.352	15.22	0.521
0.55	-28.83	0.324	23.68	0.571
0.65	-33.11	0.282	32.36	0.641
0.75	-35.25	0.232	38.46	0.729
0.85	-30.77	0.195	36.03	0.807
0.95	-14.33	0.190	17.51	0.835
1.00	0.00	0.192	0.00	0.835
	azimuthal velocity component v_θ^*			
	symmetry plane		perpendicular plane	
r^*	$v_\theta^* \pm 2.9\%$	$\Theta \pm 0.53\%$	$v_\theta^* \pm 2.9\%$	$\Theta \pm 0.53\%$
0.00	0.00	0.394	0.00	0.394
0.05	0.11	0.393	-0.11	0.398
0.15	0.34	0.388	-0.29	0.423
0.25	0.56	0.380	-0.42	0.454
0.35	0.78	0.369	-0.54	0.484
0.45	0.95	0.352	-0.66	0.520
0.55	0.08	0.324	-0.77	0.571
0.65	1.15	0.282	-0.81	0.641
0.75	1.15	0.232	-0.69	0.729
0.85	1.03	0.195	-0.38	0.807
0.95	0.54	0.190	-0.04	0.835
1.00	0.00	0.192	0.00	0.835

Table 3.9: Case B2: Rayleigh-Bénard convection. $Ra = 15000$. Numerical solutions and uncertainty estimates. Non-dimensional radial velocity and temperature for the flow symmetry plane and for its perpendicular one.

Further results

Taking into account the computational cost for solving three-dimensional domains, sometimes the hypothesis of axisymmetric flow (r-z) seems to be appropriate to obtain computational time savings. In this sense, and in order to investigate the influence of this assumption in the numerical solutions, the studied range of Rayleigh numbers has also been solved under this hypothesis. The Nusselt number has been taken as a representative solution variable. Nusselt number has been defined as:

$$\overline{Nu} = \frac{4(H/D)^2}{\pi} \int\limits_{0}^{0.5D/H} \int\limits_{0}^{2\pi} r^* \left(\frac{\partial T^*}{\partial z^*}\right)_{z^*=0,H} dr^* d\theta \qquad (3.13)$$

The results of the Nusselt number as a function of the Rayleigh number obtained with the assumption of three-dimensional and axisymmetric flow configurations are shown in Table 3.10. For Rayleigh numbers up to $Ra = 8000$, coincident results of the Nusselt number have been obtained. This agree with the previous results, where axisymmetric flow patterns have been observed. In this range ($Ra = 2200 \div 8000$), as has been commented before, azimuthal velocity can be considered negligible respect to v_r^* and v_z^* velocity components, being acceptable the hypothesis of axisymmetric flow. Beyond $Ra = 8000$, fluid bifurcates to a non-axisymmetric flow pattern, and Nusselt number considering 3D flow is greater than the calculated for the axisymmetric hypothesis.

Ra	3D	Axisymmetric
2200	1.0000	1.0000
2800	1.1773	1.1775
3000	1.2378	1.2377
4000	1.4931	1.4931
5000	1.6855	1.6855
6000	1.8343	1.8344
8000	2.0522	2.0522
15000	2.6506	2.4672

Table 3.10: Case B2: Rayleigh-Bénard problem. 3D vs. axisymmetric computations. Nusselt number for different Rayleigh numbers. $Pr = 6.7$ and aspect ratio $A = 0.5$. Level of refinement $n = 112$.

The values of the mean Nusselt number has been also compared with the obtained by Müller [14]. These results are shown in Fig. 3.14. Differences between the present work and the reported by [14] are possibly due to the numerical errors of a
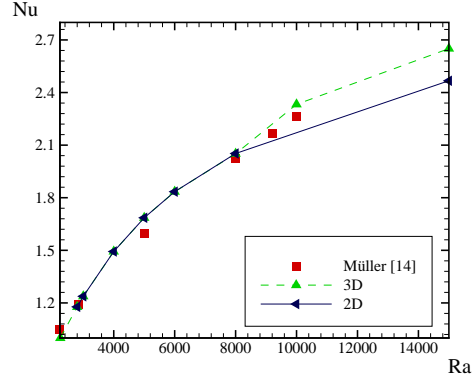
Figure 3.14: Case B2: Rayleigh-Bénard convection. Mean Nusselt number as a function of Rayleigh number for $H/D = 0.5$.

too-coarse grid used still far of a mesh independent solution (the grid used in [14] was a regular mesh of 24 mesh points in each direction).

3.3.3 Case B3: Laminar Couette flow with Taylor vortices.

This case is similar to the laminar Couette flow described before (Case A2). Two concentric cylinders of radius r_i and r_o, corresponding to the inner and outer radio respectively, and height H, one of both rotating with certain velocity (see Fig. 3.3). For the particular case of the outer cylinder fixed, Taylor [22] examined the fluid instabilities and found, following the linear theory, that as the inner cylinder velocity increases, a cellular pattern developed, in which the fluid traveled around the cylinder in vortices. He proposed a parameter to characterise this instability criterion. There are many definitions for the Taylor's number, here we use:

$$Ta = \frac{\omega_i(r_0 - r_i)}{\nu}\sqrt{\frac{r_0 - r_i}{r_i}} \tag{3.14}$$

where ω_i is the angular velocity of the inner cylinder of radius r_i. Taylor found for the geometry of his study case, that formations of vortices occurs for $Ta > 41.3$ and the transition to turbulence does not appear until $Ta = 1708$.

The instabilities that appear in the fluid are due to the destabilising effect of the centrifugal force, being in competition with the effect stabilising of the viscous drag force. The gradient of centrifugal force due to variations of kinetic momentum give

velocity gradients, so rolls appear inside the fluid if centrifugal force is greater than viscous drag force. The steady state fluid pattern is characterised by the formation of vortices in the axial plane [11, 12].

The onset of the Taylor vortices instabilities (Ta_{cr}) depends not only on the Taylor number but also on the cylinders angular velocity ratio ω_o/ω_i, on the aspect ratio $H/(r_o - r_i)$ and on the radius ratio r_i/r_o.

The boundary conditions that defines this case are:

$$
\left.\begin{aligned}
v_r &= 0 \\
v_\theta &= r_i\,\omega_i \\
v_z &= 0
\end{aligned}\right\} \text{ for } r = r_i; \forall \{\theta, z\}
\tag{3.15}
$$

$$
\left.\begin{aligned}
v_r &= 0 \\
v_\theta &= 0 \\
v_z &= 0
\end{aligned}\right\} \text{ for } r = r_0; \forall \{\theta, z\}
\tag{3.16}
$$

$$
\frac{\partial \phi}{\partial \mathbf{n}} = 0 \qquad \text{ for } z = 0\,; z = H; \forall \{r_i < r < r_0, \theta\}
\tag{3.17}
$$

In the present study, the case have been solved for a Taylor number of $Ta = 100$, an aspect ratio of $H/(r_o - r_i) = 7.5$ and for a radius ratio of $r_i/r_o = 0.5$.

Due to the complex configuration of the flow at the r-z plane, and with the objective of selecting an appropriate discretisation, it has been necessary to consider previously several discretisation meshes. In this sense, the post-processing procedure described in section 2.4 has been very helpful. For the selected discretisation mesh, more nodes in the axial direction than in the other ones, have been introduced. The mesh has been also intensified at the end walls where the variables gradients are the largest. In this zone, near the end walls, the mesh has been concentrated by means of a tanh-like function with a concentration factor of 1.

The *h-refinement* study has been performed for meshes of $(5/4n)$xnx$(2n)$ control volumes. Considering the high number of control volumes to solve accurately the case, four levels of refinement, instead of five has been considered ($n = 8, 16, 32$ and 64). The SMART scheme has been used to evaluate convective terms while the central different scheme has been used for the diffusive ones.

grid	v_r^*			v_z^*			v_θ^*		
	Rn	p	GCI	Rn	p	GCI	Rn	p	GCI
$n_3/n_2/n_1$	[%]		[%]	[%]		[%]	[%]		[%]
8/16/32	72	2.5	0.11	70	2.2	0.27	65	3.1	0.12
16/32/64	92	1.7	0.08	87	1.8	0.11	92	1.9	0.13

Table 3.11: Case B3: Laminar Couette flow with Taylor vortices. Post-processing verification results. Numerical scheme SMART for convective terms and central differences for diffusive terms.).
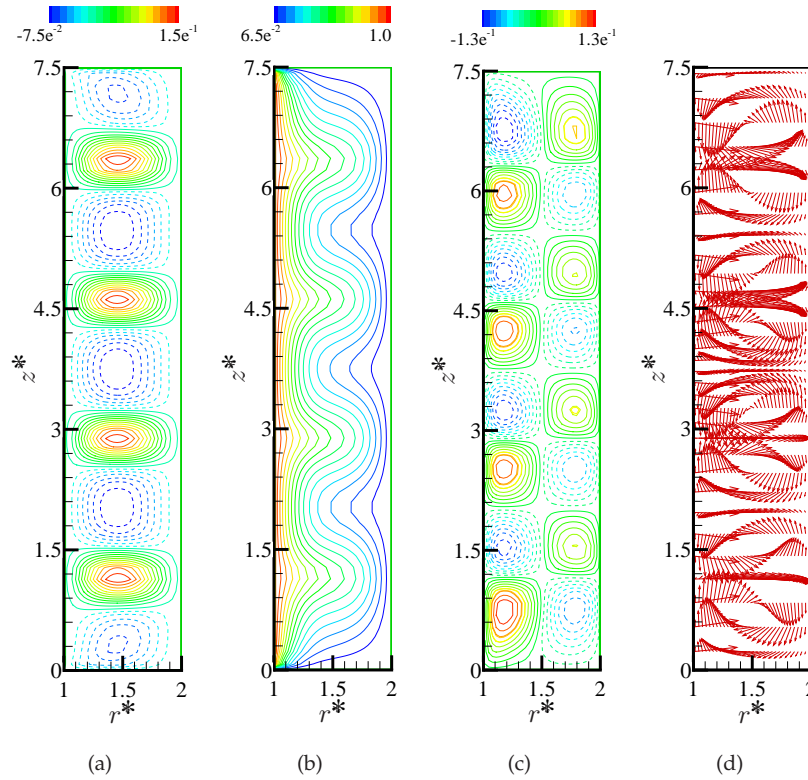

Figure 3.15: Case B3: Laminar Couette flow with Taylor vortices. Illustrative flow pattern. (a) Radial velocity component v_r^*, (b) Azimuthal velocity component v_θ^*, (c) Axial velocity component v_z^*, and (d) Velocity vector. All the plots are for an arbitrary axial plane.
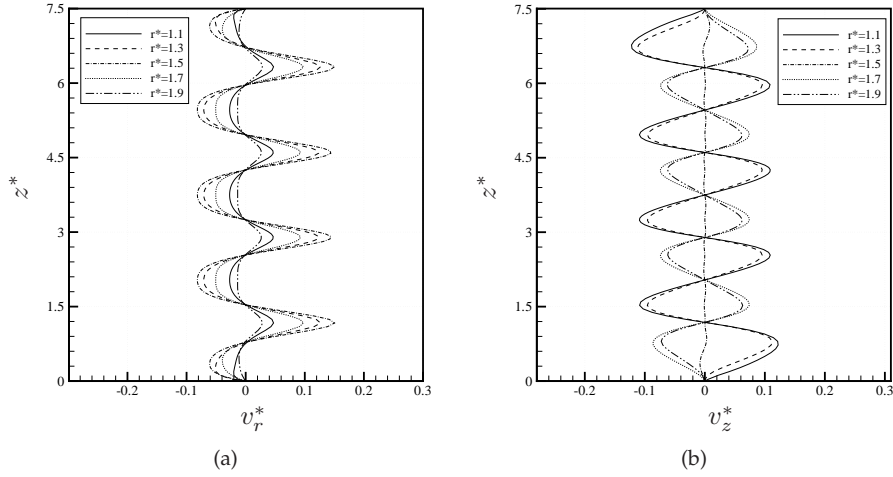
Figure 3.16: Case B3: Laminar Couette flow with Taylor vortices. Axial profiles at five non-dimensional radial positions. Level of refinement $n = 64$. (a) Non-dimensional radial velocity (b) Non-dimensional axial velocity.

The boundary conditions imposed and geometry selected, force the formation of Taylor vortices in the axial plane. When the steady state is reached, the flow configuration is axisymmetric. Azimuthal velocity of the inner cylinder has been taken as the reference velocity in the variables normalisation. Thus, non-dimensional velocities are: $v_r* = v_r/(r_i\omega_i)$, $v_\theta* = v_\theta/(r_i\omega_i)$, $v_z* = v_z/(r_i\omega_i)$. The non-dimensional radius and height have been normalised by using as reference length the annulus gap, that is: $r^* = r/(r_o - r_i)$ and $z^* = z/(r_o - r_i)$.

The results of the verification post-process are given in Table 3.11. For the finest mesh, a high level of Richardson nodes for all variables has been achieved, being the order of accuracy of the solution greater than 1.7 (order of accuracy for SMART scheme between $1 \div 3$). The GCI also shows a good behaviour, for all variables.

Being the solution axisymmetric, the steady state non-dimensional velocity components profiles and velocity vector for an arbitrary plane in the azimuthal direction are shown Fig. 3.15. In this figure, the effects of the boundary conditions imposed at the end walls ($z^* = 0; 7.5$), can be observed. Notice also, that the fluid vortices are anti-symmetric respect to middle plane of the cylinder ($z^* = 3.75$). This can also be observed in Fig. 3.16, where the axial profiles for v_r^* and v_z^* are plotted at radial positions of $r^* = 1.1$, 1.3, 1.5, 1.7 and 1.9, for the finest mesh (level of refinement

$n = 64$). The values of the non-dimensional variables along these radial positions, together with their uncertainties estimators, are given in Table 3.12.

			$v_r^* \pm 0.08\%$		
z^*	$r^* = 1.1$	$r^* = 1.3$	$r^* = 1.5$	$r^* = 1.7$	$r^* = 1.9$
0.375	−0.0169	−0.0492	−0.0609	−0.0393	−0.0109
1.125	0.0451	0.1216	0.1451	0.0948	0.0274
1.875	−0.0252	−0.0664	−0.0778	−0.0494	−0.0136
2.625	0.0132	0.0348	0.0418	0.0270	0.0741
3.375	−0.0137	−0.0372	−0.0453	−0.0306	−0.0920
4.125	−0.0137	−0.0372	−0.0453	−0.0306	−0.0920
4.875	0.0132	0.0348	0.0418	0.0270	0.0741
5.625	−0.0252	−0.0664	−0.0778	−0.0494	−0.0136
6.375	0.0451	0.1216	0.1451	0.0948	0.0274
7.125	−0.0169	−0.0492	−0.0609	−0.0393	−0.0109
			$v_z^* \pm 0.11\%$		
z^*	$r^* = 1.1$	$r^* = 1.3$	$r^* = 1.5$	$r^* = 1.7$	$r^* = 1.9$
0.375	0.0616	0.0563	0.0010	−0.0436	−0.0359
1.125	0.0073	0.0083	0.0005	−0.0067	−0.0043
1.875	−0.0225	−0.0213	−0.0014	0.0151	0.0156
2.625	0.0051	0.0032	−0.0002	−0.0041	−0.0007
3.375	−0.0267	−0.0236	0.0007	0.0176	0.0154
4.125	0.0267	0.0236	−0.0007	−0.0176	−0.0154
4.875	−0.0051	−0.0032	0.0002	0.0041	0.0007
5.625	0.0225	0.0213	0.0014	−0.0151	−0.0156
6.375	−0.0073	−0.0083	−0.0005	0.0067	0.0043
7.125	−0.0616	−0.0563	−0.0010	0.0436	0.0359
			$v_\theta^* \pm 0.13\%$		
z^*	$r^* = 1.1$	$r^* = 1.3$	$r^* = 1.5$	$r^* = 1.7$	$r^* = 1.9$
0.375	0.6541	0.2584	0.1621	0.1115	0.0392
1.125	0.8516	0.6381	0.5057	0.3853	0.1485
1.875	0.7110	0.3387	0.2089	0.1342	0.0471
2.625	0.7947	0.5213	0.4124	0.3157	0.1178
3.375	0.7400	0.4063	0.2968	0.2164	0.0782
4.125	0.7400	0.4063	0.2968	0.2164	0.0782
4.875	0.7947	0.5213	0.4124	0.3157	0.1178
5.625	0.7110	0.3387	0.2089	0.1342	0.0471
6.375	0.8516	0.6381	0.5057	0.3853	0.1485
7.125	0.6541	0.2584	0.1621	0.1115	0.0392

Table 3.12: Case B3: Laminar Couette flow with Taylor vortices. Numerical solutions and uncertainty estimates for non-dimensional radial, axial and azimuthal velocities at different non-dimensional radius. Level of refinement $n = 64$.

3.4 Conclusions

The aim of this chapter has been three-fold: to verify the code developed in order to solve cases in three-dimensional cylindrical coordinate domains, to test the post-processing procedure for the verification of the numerical solutions and, to obtain verified solutions of test cases in this kind of domains. In this sense, different cases in two and three-dimensional cylindrical coordinates have been presented. The numerical solution of the cases analysed have been submitted to a detailed process of verification. Two main aspects have been emphasized: i) the use of the post-processing procedure in the process of the code verification pointing out its utility in the selection of the appropriate discretisation and numerical schemes employed and; ii) the applicability of this procedure in the numerical solution verification of three-dimensional cylindrical coordinates problems.

In two of the cases presented (case A1 and cas A2), both with analytical solution, the estimators obtained have been compared with the exact discretisation error showing a good prediction of this value by the CGI for a high number of Richardson nodes. Furthermore, the order of accuracy has shown a trend to its theoretical value. This also gives criteria about the appropriateness of this procedure for the verification of three-dimensional cylindrical coordinates CFD simulations. The detailed process of verification has been useful in order to select an appropriate mesh distribution and also in detecting programming bugs during the process of code development.

Solutions of three selected CFD and heat transfer problems have been also presented: an induced flow by a tangential velocity at the boundary, the Rayleigh-Bénard problem and the laminar Couette flow with Taylor vortices. Each problem has been described in detail and the most relevant numerical solutions for the velocity and temperature fields, together with their uncertainty estimators have been provided. In all cases, the estimators obtained have shown a good behaviour with a high percentage of Richardson nodes and an order of accuracy of the solution around its theoretical value. Verified numerical solutions for three-dimensional cylindrical problems presented, can be used as reference solutions in the process of verification of CFD and heat transfer codes.

Nomenclature

D	cylinder diameter (m)	Ra	Rayleigh number
e_D	exact global discretisation error (%)	Re	Reynolds number

GCI	Grid Convergence Index (%)	Rn	Richardson nodes (%)
g	acceleration of gravity (m/s^2)	T	temperature (K)
H	cylinder height (m)	T_0	initial temperature (K)
n	grid parameter	Ta	Taylor number
Nu	Nusselt number	T_{ref}	reference temperature (K)
p	observed order of accuracy	u	magnitude of velocity vector (m/s)
Pr	Prandtl number	v_r	radial velocity component (m/s)
R	cylinder radius (m)	v_θ	azimuthal velocity component (m/s)
r_i	inner cylinder radius (m)	v_z	axial velocity component (m/s)
r_o	outer cylinder radius (m)	z	axial coordinate (m)
r	radial coordinate (m)		

greeks

α	thermal diffusivity (m^2/s)	ρ	density (kg/m^3)
β	thermal expansion coefficient (K^{-1})	ω	angular velocity (s^{-1})
η	radius ratio	ω_i	inner cylinder angular velocity (s^{-1})
μ	dynamic viscosity (kg/ms)	ω_o	outer cylinder angular velocity (s^{-1})
Θ	Non-dimensional temperature	θ	azimuthal coordinate (rad)

References

[1] P.J. Roache. Verification of codes and calculations. *AIAA Journal*, 36(5):696–702, 1998.

[2] I. P. Jones. A Comparison Problem for Numerical Methods in Fluids Dynamics: The "Double-Spacing" Problem. In *Proceedings of the 9th Conference on Numerical Methods in Thermal Problems*, pages 338–348, 1979.

[3] G. De Vahl Davis and I.P. Jones. Natural convection in a square cavity: a comparison exercise. *International Journal for Numerical Methods in Fluids*, 3:227–248, 1983.

[4] G. De Vahl Davis. Natural convection of air in a square cavity: a benchmark numerical solution. *International Journal for Numerical Methods in Fluids*, 3:249–264, 1983.

References

[5] K. Salari and P. Knupp. Code verification by the method of manufactured solutions. Technical report, Sandia National Laboratories, 2000.

[6] W. L. Oberkamp and T. G. Trucano. Verification and validation in Computational Fluid Dynamics. Technical report, Sandia National Laboratories, 2002.

[7] P.J. Roache. Code verification by the method of manufactured solutions. *Journal of Fluids Engineering*, 124:4–10, 2002.

[8] P.J. Roache. Perspective: a method for uniform reporting of grid refinement studies. *Journal of Fluids Engineering*, 116:405–413, 1994.

[9] R. Becker and R. Rannacher. A feed-back approach to error control in finite element methods: Basic analysis examples. *Journal of Numerical Mathematics*, (41):428–439, 1996.

[10] J. Cadafalch, C.D. Pérez-Segarra, R. Cònsul, and A. Oliva. Verification of finite volume computations on steady state fluid flow and heat transfer. *Journal of Fluids Engineering*, 124:11–21, 2002.

[11] H. Schlichting. *Teoría de la capa límite*. Ediciones Urmo, 1972.

[12] E.L. Koschmieder. *Benard cells and taylor vortices*. Press Syndicate of the University of Cambridge, 1993.

[13] R.M. Smith and A.G. Hutton. The numerical treatment of advection: a performance comparison of current methods. *Numerical Heat Transfer*, 5:439–461, 1982.

[14] G. Müller, G. Neumann, and W. Weber. Natural convection in vertical bridgman configurations. *Journal of Crystal Growth*, 70:78–93, 1984.

[15] G. Neumann. Three-dimensional numerical simulation of buoyancy-driven convection in vertical cylinders heated from below. *Journal of Fluid Mechanics*, 214:559–578, 1990.

[16] G. De Vahl Davis. A note on a mesh for use with polar coordinates. *Numerical Heat Transfer*, 2:261–266, 1979.

[17] C.D Andereck, S.S Liu, and Swinney H.L. Flow regimes in a circular couette system with independing rotating cylinders. *J. Fluid Mechanics*, 164:155–183, 1986.

[18] C.B. Liao, S.J. Jane, and D.L. Young. Numerical simulation of three-dimensional couette-taylor flows. *International Journal for Numerical Methods in Fluids*, 29:827–847, 1999.

[19] S. Rosenblat. Thermal convection in a vertical circular cylinder. *Journal of Fluids Mechanics*, 122:395–410, 1982.

[20] S. Schneider and J. Straub. Laminar natural convection in a cylindrical enclosure with different end temperature. *International Journal of Heat and Mass Transfer*, 35(2):545–557, 1992.

[21] J.C. Buell and I. Catton. The effect of wall conduction on the stability of a fluid in a right circular cylinder heated from below. *Journal of Heat Transfer*, 105:255–260, 1983.

[22] Taylor G.I. Stability of viscous liquids contained between two rotating cylinders. *Phil. Trans. R. Soc. London*, 223:289, 1923.